










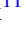











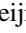
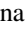

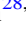
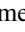
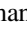







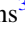








JWST NIRSpec Spectroscopy of the Triply Lensed $z = 10.17$ Galaxy MACS0647–JD

Tiger Yu-Yang Hsiao^{1,2,3,37} , Abdurro'uf^{1,2,3,37} , Dan Coe^{1,2,3,4} , Rebecca L. Larson⁵ , Intae Jung³ , Matilde Mingozzi³ ,
 Pratika Dayal⁶ , Nimisha Kumari^{3,4} , Vasily Kokorev⁷ , Anton Vikaeus⁸ , Gabriel Brammer^{9,10} , Lukas J. Furtak¹¹ ,
 Angela Adamo¹² , Felipe Andrade-Santos^{1,13,14} , Jacqueline Antwi-Danso^{15,16,17} , Maruša Bradač^{18,19} ,
 Larry D. Bradley³ , Tom Broadhurst^{20,21,22} , Adam C. Carnall²³ , Christopher J. Conselice²⁴ , Jose M. Diego²⁵ ,
 Megan Donahue²⁶ , Jan J. Eldridge²⁷ , Seiji Fujimoto^{7,38} , Alaina Henry^{2,3} , Svea Hernandez^{3,4} ,
 Taylor A. Hutchison^{28,39} , Bethan L. James^{3,4} , Colin Norman^{2,3} , Hyunbae Park²⁹ , Norbert Pirzkal³ , Marc Postman³ ,
 Massimo Ricotti³⁰ , Jane R. Rigby²⁸ , Eros Vanzella³¹ , Brian Welch^{28,30} , Stephen M. Wilkins^{32,33} ,
 Rogier A. Windhorst³⁴ , Xinfeng Xu^{35,36} , Erik Zackrisson⁸ , and Adi Zitrin¹¹ 

¹ Center for Astrophysics | Harvard & Smithsonian, 60 Garden Street, Cambridge, MA 02138, USA

² Center for Astrophysical Sciences, Department of Physics and Astronomy, The Johns Hopkins University, 3400 N Charles St. Baltimore, MD 21218, USA;

tiger.hsiao@cfa.harvard.edu, fabdurr1@jhu.edu

³ Space Telescope Science Institute, 3700 San Martin Drive, Baltimore, MD 21218, USA

⁴ Association of Universities for Research in Astronomy (AURA), Inc. for the European Space Agency (ESA), USA

⁵ School of Physics and Astronomy, Rochester Institute of Technology, 84 Lomb Memorial Drive, Rochester, NY 14623, USA

⁶ Kapteyn Astronomical Institute, University of Groningen, P.O. Box 800, 9700AV Groningen, The Netherlands

⁷ The University of Texas at Austin, Department of Astronomy, Austin, TX, USA

⁸ Observational Astrophysics, Department of Physics and Astronomy, Uppsala University, Box 516, SE-751 20 Uppsala, Sweden

⁹ Cosmic Dawn Center (DAWN), Copenhagen, Denmark

¹⁰ Niels Bohr Institute, University of Copenhagen, Jagtvej 128, Copenhagen, Denmark

¹¹ Physics Department, Ben-Gurion University of the Negev, P.O. Box 653, Be'er-Sheva 84105, Israel

¹² Department of Astronomy, Oskar Klein Centre, Stockholm University, AlbaNova University Centre, SE-106 91 Stockholm, Sweden

¹³ Department of Liberal Arts and Sciences, Berklee College of Music, 7 Haviland Street, Boston, MA 02215, USA

¹⁴ Clay Center Observatory, Dexter Southfield, 20 Newton Street, Brookline, MA 02445, USA

¹⁵ George P. and Cynthia Woods Mitchell Institute for Fundamental Physics and Astronomy, Texas A&M University, College Station, TX 77743, USA

¹⁶ Department of Physics and Astronomy, Texas A&M University, 4242 TAMU, College Station, TX 77743, USA

¹⁷ Department of Astronomy & Astrophysics, University of Toronto, Toronto, Ontario M5S 3H4, Canada

¹⁸ Department of Mathematics and Physics, University of Ljubljana, Jadranska ulica 19, SI-1000 Ljubljana, Slovenia

¹⁹ Department of Physics and Astronomy, University of California, Davis, 1 Shields Ave, Davis, CA 95616, USA

²⁰ Department of Theoretical Physics, University of the Basque Country, UPV-EHU, E-48040 Bilbao, Spain

²¹ Donostia International Physics Center (DIPC), 20018 Donostia, The Basque Country, Spain

²² IKERBASQUE, Basque Foundation for Science, Alameda Urquijo 36-5, E-48008 Bilbao, Spain

²³ Institute for Astronomy, University of Edinburgh, Royal Observatory, Edinburgh EH9 3HJ, UK

²⁴ Jodrell Bank Centre for Astrophysics, University of Manchester, Oxford Road, Manchester M13 9PL, UK

²⁵ Instituto de Física de Cantabria (CSIC-UC), Avda. Los Castros s/n. 39005 Santander, Spain

²⁶ Michigan State University, Physics & Astronomy Department, East Lansing, MI, USA

²⁷ Department of Physics, University of Auckland, Private Bag 92019, Auckland, New Zealand

²⁸ Observational Cosmology Lab, NASA Goddard Space Flight Center, Greenbelt, MD 20771, USA

²⁹ Lawrence Berkeley National Laboratory, CA 94720, USA

³⁰ Department of Astronomy, University of Maryland, College Park, 20742, USA

³¹ INAF—OAS, Osservatorio di Astrofisica e Scienza dello Spazio di Bologna, via Gobetti 93/3, I-40129 Bologna, Italy

³² Astronomy Centre, University of Sussex, Falmer, Brighton BN1 9QH, UK

³³ Institute of Space Sciences and Astronomy, University of Malta, Msida MSD 2080, Malta

³⁴ School of Earth and Space Exploration, Arizona State University, Tempe, AZ 85287-6004, USA

³⁵ Department of Physics and Astronomy, Northwestern University, Evanston, IL, 60208, USA

³⁶ Center for Interdisciplinary Exploration and Research in Astrophysics (CIERA), Northwestern University, Evanston, IL, 60201, USA

Received 2023 May 4; revised 2024 June 19; accepted 2024 June 27; published 2024 September 11

Abstract

We present JWST/NIRSpec prism spectroscopy of MACS0647–JD, a triply lensed $z \sim 11$ candidate discovered in Hubble Space Telescope imaging and spatially resolved by JWST imaging into two components, A and B. Spectroscopy of component A yields a spectroscopic redshift $z = 10.17$ based on seven detected emission lines: C III] $\lambda\lambda 1907, 1909$, [O II] $\lambda 3727$, [Ne III] $\lambda 3869$, [Ne III] $\lambda 3968$, H δ $\lambda 4101$, H γ $\lambda 4340$, and [O III] $\lambda 4363$. These are the second-most distant detections of these emission lines to date, in a galaxy observed just 460 million years after the Big Bang. Based on observed and extrapolated line flux ratios we derive a gas-phase metallicity $12 + \log(\text{O}/\text{H}) \sim 7.5\text{--}8.0$, or $Z \sim (0.06\text{--}0.2) Z_{\odot}$, ionization parameter $\log(U) = -1.9 \pm 0.2$, and an ionizing photon

³⁷ Both lead authors contributed equally.

³⁸ Hubble Fellow.

³⁹ NASA Postdoctoral Fellow.

production efficiency $\log(\xi_{\text{ion}}) = 25.2 \pm 0.2 \text{ erg}^{-1} \text{ Hz}$. The spectrum has a softened Ly α break, evidence for a strong Ly α damping wing. The Ly α damping wing also suppresses the F150W photometry, explaining the slightly overestimated photometric redshift $z = 10.6 \pm 0.3$. MACS0647–JD has a stellar mass $\log(M/M_{\odot}) = 8.1 \pm 0.3$, including $\sim 6 \times 10^7 M_{\odot}$ in component A, most of which formed recently (within ~ 20 Myr) with a star formation rate $\sim 2 \pm 1 M_{\odot} \text{ yr}^{-1}$, all within an effective radius 70 ± 24 pc. Spectroscopy of a fainter companion galaxy C separated by a distance of ~ 3 kpc reveals a Lyman break consistent with $z \sim 10.17$. MACS0647–JD is likely the most distant galaxy merger known.

Unified Astronomy Thesaurus concepts: Galaxies (573); High-redshift galaxies (734); Early universe (435); Strong gravitational lensing (1643); Galaxy spectroscopy (2171); Reionization (1383)

1. Introduction

Spectroscopy using the NIRSpec instrument (Ferruit et al. 2022; Jakobsen et al. 2022; Böker et al. 2023) on board JWST (Gardner et al. 2023; Rigby et al. 2023) is beginning to confirm distant galaxy candidates and reveal their properties in the early Universe ($z > 8$; e.g., Arrabal Haro et al. 2023a; Bunker et al. 2023; Curtis-Lake et al. 2023; Fujimoto et al. 2023; Roberts-Borsani et al. 2023; Harikane et al. 2024). With coverage out to $5.3 \mu\text{m}$, NIRSpec can detect the strong emission lines [O III] $\lambda\lambda 4959, 5007$ and H β in galaxies as distant as $z \sim 9.5$, confirming redshifts and constraining properties such as metallicity and ionization parameter when combined with other emission lines (e.g., Cameron et al. 2023b; Nakajima et al. 2023; Tang et al. 2023; Williams et al. 2023; Boyett et al. 2024; Jung et al. 2024; Sanders et al. 2024).

At $z > 10$, within the first 500 million years, spectroscopic confirmations and detailed studies are more challenging because [O III] + H β is redshifted out of the NIRSpec wavelength range, and fainter emission lines are difficult to detect in low-luminosity $z > 10$ galaxies. Brighter galaxies or longer exposure times are required. Curtis-Lake et al. (2023) presented deep spectra with a spectral resolution of $R \sim 100$ that impressively confirmed galaxies with redshifts $z = 10.4, 11.6, 12.6,$ and 13.2 based on significant Lyman break detections and an absence of definitive emission lines in long exposures of 9–28 hr for these faint candidates (F200W AB mag 28–29). Similarly, Arrabal Haro et al. (2023a) confirmed galaxies at $z = 10.1$ and $z = 11.4$ based on Lyman break detections with no emission lines in 5 hr NIRSpec prism spectra that also revised the redshift of a $z \sim 16$ candidate down to $z = 4.912$.

Over a decade of Hubble Space Telescope (HST) WFC3/IR observations yielded two $z > 10$ galaxies bright enough (F200W AB mag 25.8 ± 0.1) for more detailed study. GN-z11 was one of the most distant galaxies ever discovered in HST imaging (Oesch et al. 2016). They noted that given the search area, it was surprising to discover a galaxy so bright. JWST NIRCам (Rieke et al. 2023) imaging photometry yields F200W AB mag of 25.9 ± 0.1 and $M_{\text{UV}} = -21.6$, or $M_{\text{UV}} = -21.8$ corrected for dust (Tacchella et al. 2023). JWST NIRSpec spectroscopy has now confirmed GN-z11 at $z = 10.603$ and revealed 12 emission lines (Bunker et al. 2023).

MACS0647–JD was the other similarly bright $z \sim 11$ candidate discovered in HST imaging (Coe et al. 2013), supported by HST grism observations (Pirzkal et al. 2015), Spitzer imaging (Lam et al. 2019), and gravitational lens modeling (Chan et al. 2017). MACS0647–JD is triply lensed by a massive foreground galaxy cluster, MACSJ0647.7+7015 ($z = 0.591$; Ebeling et al. 2007). Despite lensing magnifications of $\sim 8, 5,$ and 2 (Meena et al. 2023), the three lensed images JD1, JD2, and JD3 were spatially unresolved in HST imaging.

JWST/NIRCам imaging resolved MACS0647–JD as having two small components in a possible galaxy merger at $z = 10.6 \pm 0.3$ (Hsiao et al. 2023). The brighter component A has an effective radius $r \sim 70 \pm 24$ pc and appears bluer, ($\beta \sim -2.6 \pm 0.1$), likely due to its young stellar population (~ 50 Myr old) and no dust. The other component, JDB, has a smaller radius of $r \sim 20_{-5}^{+8}$ pc and appears redder ($\beta \sim -2 \pm 0.2$), likely due to an older stellar population (~ 100 Myr old) and mild dust ($A_V \sim 0.1$ mag). The different inferred star formation histories (SFHs) suggest these two components formed separately and are in the process of merging. A third triply lensed component C was also identified $2''$ away (~ 3 kpc in the deconvolved source plane). With similar colors and a consistent photometric redshift, C may be destined to merge with A and B.

Compared to GN-z11, MACS0647–JD is intrinsically fainter ($M_{\text{UV}} = -20.3$), yet observed to be brighter; the brightest lensed image JD1 is F200W AB mag 25.0 ± 0.1 . The brightest clump A is $M_{\text{UV}} = -19.5$ and lensed to F200W AB mag of 25.8 ± 0.1 in JD1. This enables detailed study with JWST.

In this paper, we report NIRSpec and NIRCам observations of MACS0647–JD obtained by JWST observation program GO 1433 (PI: Coe). Most of the NIRCам images were analyzed previously by Hsiao et al. (2023). This work includes a new F480M image, deeper F200W data, and updated image reductions and photometry (Section 2). Based on NIRSpec prism ($R \sim 100$) spectroscopy spanning $0.7\text{--}5.3 \mu\text{m}$, we detect nebular emission lines, measure the spectroscopic redshift, and derive physical properties including the ionization parameter and metallicity using various emission line ratios as well as photometric spectral energy distribution (SED) fitting (Section 3). We present conclusions in Section 4.

2. Observations

JWST program GO 1433 (PI: Coe) observed MACS0647–JD as summarized in Table 1. We also analyze archival HST imaging from programs GO 9722, 10493, 10793, 12101, and 13317, described in Hsiao et al. (2023). All JWST and HST data are publicly available in the Mikulski Archive for Space Telescopes (MAST; doi:10.17909/wpys-ap03). We also provide reduced data products⁴⁰ along with our data analysis scripts.⁴¹

2.1. NIRSpec MOS Prism Spectroscopy

There were two separate NIRSpec multiobject spectroscopy (MOS) observations (Obs 21 and Obs 23) using the microshutter assembly (MSA). Both used the low-resolution $R \sim 30\text{--}300$ prism yielding data from 0.6 to $5.3 \mu\text{m}$. Obs 23 was performed with standard three slitlet nods used to subtract

⁴⁰ <https://cosmic-spring.github.io>

⁴¹ <https://github.com/cosmic-spring/MACS0647-JD-NIRSpec>

Table 1
JWST Observations of MACS0647–JD

Observation	Date (UT)	Mode	Exposures	Filters / Element	Exposure Time ^a
10	2022-09-23	NIRCam imaging	Three filter pairs	F115W, F150W, F200W, F277W, F356W, F444W	2104 s
20	2023-01-08	NIRCam imaging	One filter pair	F200W, F480M	2104 s
21	2023-01-08	NIRSpec MOS	One slitlet; two dithers ^b	prism	6420 s
23	2023-02-20	NIRSpec MOS	Three slitlet nods	prism	6567 s

Notes.

^a Exposure time per imaging filter; total exposure times for NIRSpec.

^b Each dither requires its own microshutter assembly (MSA) configuration.

backgrounds measured near each target. The total exposure time was 1.8 hr. Obs 21 was performed with single slitlets, requiring backgrounds to be measured in nearby slitlets designed to observe “blank” sky and intracluster light. Two MSA configurations were executed in Obs 21 with a total exposure time of 1.8 hr. The two configurations were similar with small dithers between them and most targets included in both.

The two brightest lensed images of MACS0647–JD (JD1 and JD2) were observed in all exposures of all observations for a total exposure time of 3.6 hr. The slitlets primarily captured light from the brightest clump A. The brightest lensed images of the companion galaxy C (JD1C and JD2C) were also observed in all exposures. Since JD1 and JD2 are multiple images of the same object with JD2 magnified $\sim 70\%$ as bright ($\mu \sim 5.3$) as JD1, the resulting summed spectra have a signal-to-noise ratio (S/N) similar to 6 hr total effective exposure times on JD1A and JD1C.

Clump B was observed only in Obs 21 of JD2. Given its proximity to clump A, it is difficult to spatially resolve its contribution to the JD2 spectrum. They are separated by only one or two $0''.1$ pixels in the cross-dispersion direction (i.e., in the 2D NIRSpec spectrum). We do perhaps detect some emission line fluxes (i.e., C III] $\lambda\lambda 1907, 1909$) from JD2B as we discuss in Section 3.4 (see also the second row of Figure 1).

We retrieved NIRSpec Level 1 data products from MAST and processed them with the STScI JWST pipeline⁴² version 1.9.2 and MSAEXP⁴³ version 0.6.0. First, MSAEXP corrects for $1/f$ noise,⁴⁴ masks snowballs,⁴⁵ corrects bias levels in individual exposures, and rescales the noise array R_{NOISE} based on measurements in blank regions. Next, we run JWST pipeline Stage 2 routines to perform world coordinate system registration, flat-fielding, pathloss corrections, and flux calibration.

For the three slitlet data, background subtraction is performed locally before drizzling the three exposures onto a common 2D pixel grid. For the single-slitlet data, we drizzle-combined data from the two exposures (MSA configurations). Then we subtracted the 2D background spectrum in a nearby slit ($\#50981$) that observed a relatively blank region of the image.

To extract each 1D spectrum, MSAEXP uses a Gaussian profile in the cross-dispersion direction, derived from an inverse-weighted sum of the 2D spectrum in the dispersion

direction, based on the optimal extraction described in Horne (1986). The results are shown in Figure 1 for each observation. The plots show the numbers for the extraction Gaussian: offset \pm width in pixels. There are no design choices to exclude any contribution from clumps A and B.

Finally, we sum the 1D spectra, adding flux uncertainties in quadrature, yielding the spectrum shown in Figure 2. This spectrum includes the total flux observed in all four exposures for JD1A and JD2A.

2.2. NIRCam Imaging

NIRCam imaging was obtained first in six filters, F115W, F150W, F200W, F277W, F356W, and F444W spanning 1–5 μm , and the results were studied and presented in Hsiao et al. (2023). Additional NIRCam imaging has since been obtained in F200W and F480M, concurrent with the NIRSpec Obs 21. The F480M observation was included to observe MACS0647–JD redward of the Balmer break to better constrain its stellar age and mass. Each NIRCam image has an exposure time of 35 minutes, split between four INTRAMODULEBOX dithers that cover the short-wavelength gaps.

We process the NIRCam images using the STScI JWST pipeline and GRIZLI (Brammer et al. 2022). In Hsiao et al. (2023), we analyzed the fourth release (v4) of the images reduced with GRIZLI and then performed zero-point corrections based on updated calibrations that remain robust today (Boyer et al. 2022). Those updated zero-points were implemented in GRIZLI v5. In this work, we analyze GRIZLI v6 image mosaics⁴⁶ featuring improved sky flats, bad pixel tables, wisp templates, and long-wavelength zero-points.

Briefly, in each NIRCam exposure, the GRIZLI pipeline applies corrections for $1/f$ noise striping and masks “snowballs”⁴⁷ and “wisps.”⁴⁸ Then GRIZLI drizzle-combines all exposures in each filter on to a common pixel grid using ASTRODRIZZLE (Koekemoer et al. 2003; Hoffmann et al. 2021). The NIRCam short-wavelength images are drizzled to $0''.02$ pixels, and all other images are drizzled to $0''.04$ pixels. All images are aligned with coordinates registered to Gaia Data Release 3 (Gaia Collaboration et al. 2021). We create color images using TRILOGY⁴⁹ (Coe et al. 2012).

We measure JWST photometry of the lensed images JD1 and JD2 using GRIZLI with circular apertures of $0''.25$ radius.

⁴² <https://github.com/spacetelescope/jwst>

⁴³ <https://github.com/gbrammer/msaexp>

⁴⁴ While the observations were obtained in IRS2 readout mode to mitigate the effect of $1/f$ noise, NIRSpec data still exhibit this characteristic to some extent, motivating the correction.

⁴⁵ Snowballs are now masked by the JWST Level 1 pipeline as well.

⁴⁶ <https://github.com/gbrammer/grizli/blob/master/docs/grizli/image-release-v6.rst>

⁴⁷ <https://jwst-docs.stsci.edu/data-artifacts-and-features/snowballs-and-shower-artifacts>

⁴⁸ <https://jwst-docs.stsci.edu/jwst-near-infrared-camera/nircam-instrument-features-and-caveats/nircam-claws-and-wisps>

⁴⁹ <https://github.com/dancoe/trilogy>

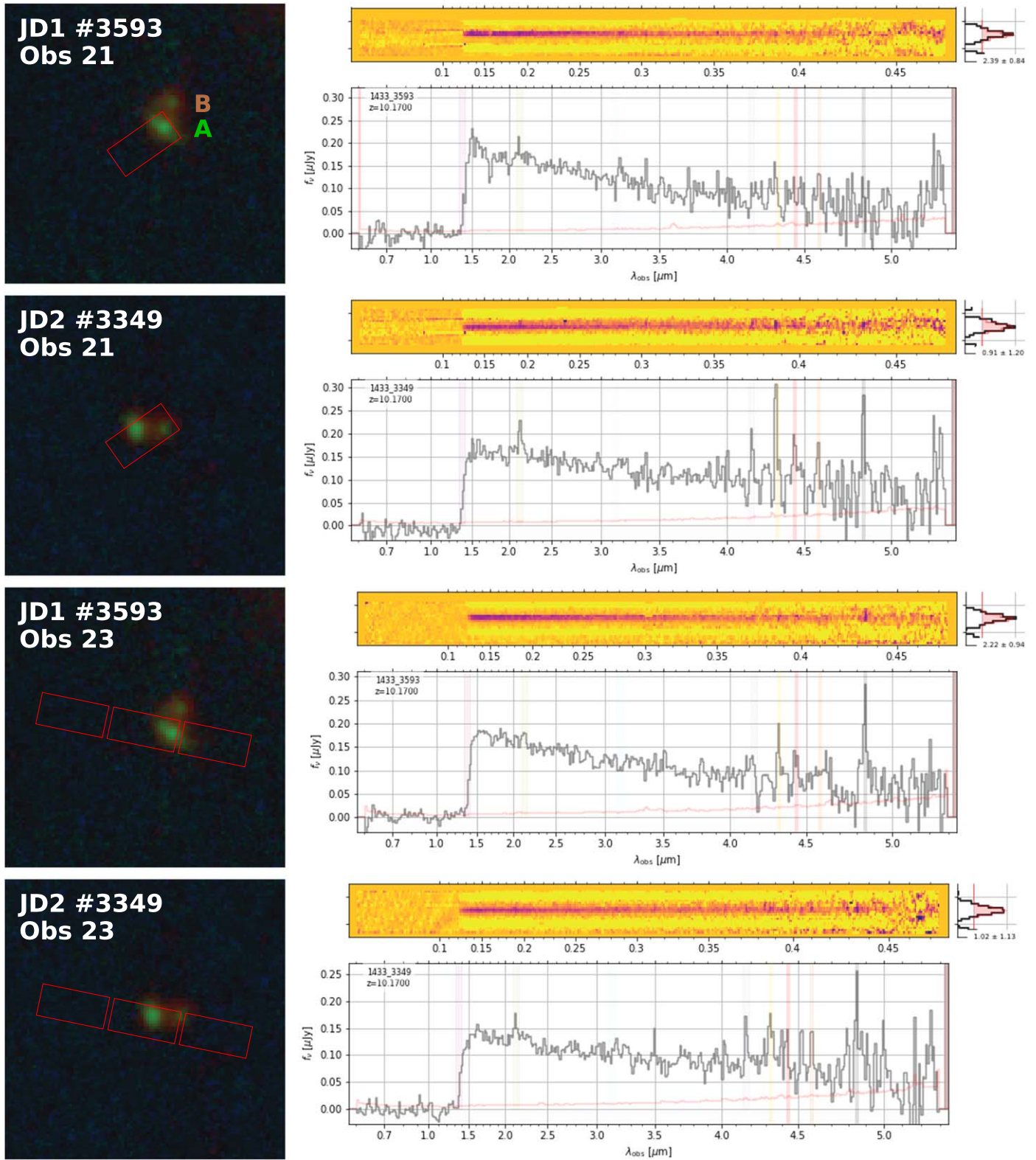


Figure 1. Individual NIRSpectra of MACS0647–JD lensed images JD1 and JD2 (#3593 and #3349, respectively, in the catalog used to prepare NIRSpect Observations 21 and 23). Left: slitlets in red are overlaid on $2'' \times 2''$ NIRCcam color images (blue: F115W; cyan: F150W; green: F200W; red: F277W, F356W, F444W, and F480M). Note that most of the observations target the brighter component A. Right: 2D spectra vs. rest-frame wavelength for $z = 10.17$ (top) and 1D spectra F_ν (μJy) vs. observed wavelength in microns (bottom). In each 1D plot, the gray line shows the spectrum, and the red line shows the uncertainty. Faint vertical colored shaded regions mark wavelengths of common emission lines: Ly α $\lambda 1216$ (pink), C III] $\lambda\lambda 1907, 1909$ (green), Mg II $\lambda 2800$ (blue), [O II] $\lambda 3727$ (purple), [Ne III] $\lambda 3869$ (yellow), [Ne III] $\lambda 3968$ (red), H δ (orange), and H γ (gray). Only two of those (C III] and [O II]) appear in MACS0647–JD, along with others revealed in the summed spectrum (Figure 2) and listed in Table 3.

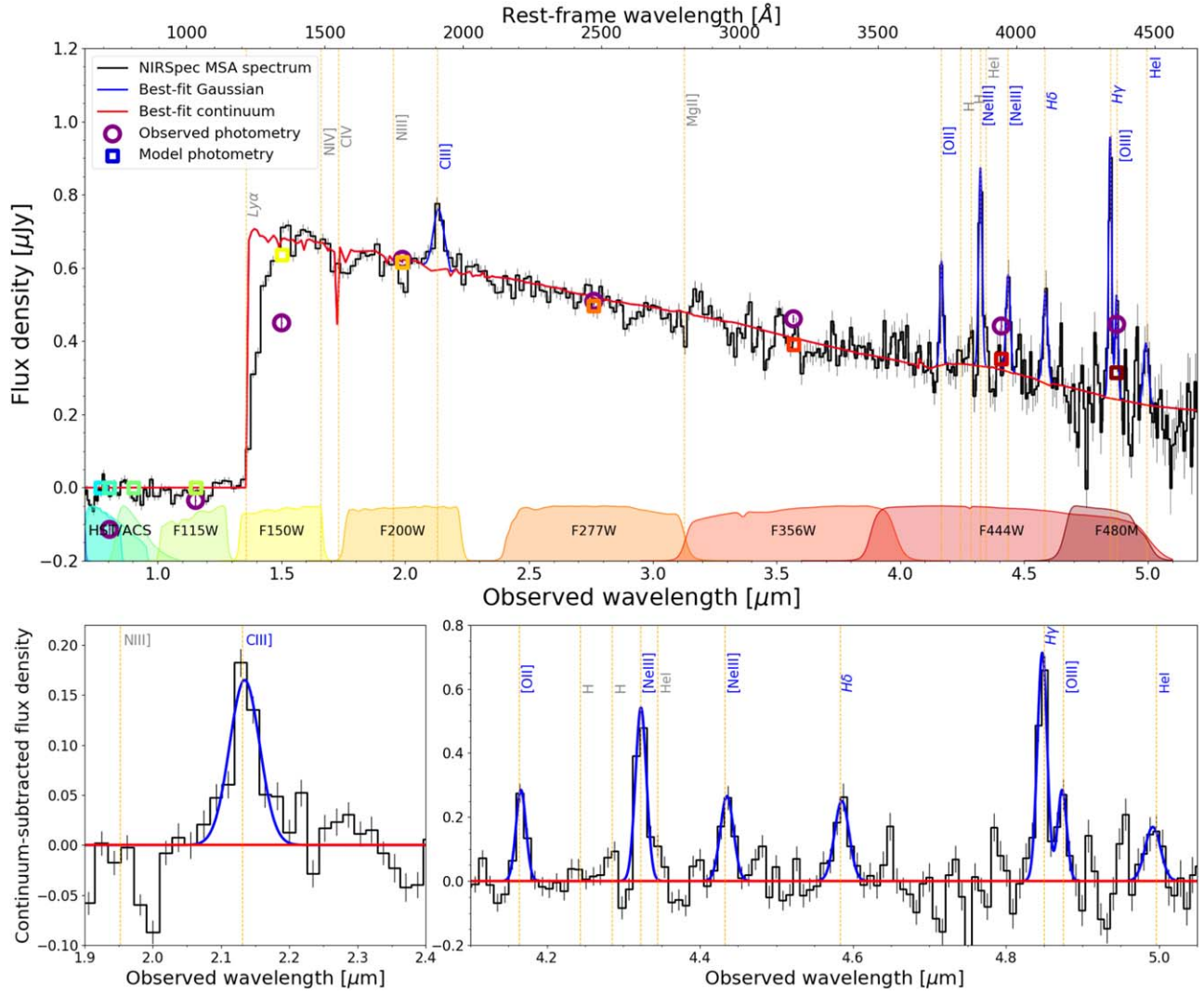


Figure 2. Spectrum and photometry of MACS0647–JD component A in the sum of both lensed images in both observations (i.e., JD1 Obs 21 + JD1 Obs 23 + JD2 Obs 21 + JD2 Obs 23), with a total magnification $\sim 26.6 = 8 + 8 + 5.3 + 5.3$. The spectrum is the sum of all four observed spectra. The photometry shown here is measured within rectangular apertures resembling the NIRSpect slits in the four exposures. The red line is the PIXEDFIT model fit to the spectrum with emission lines masked out. After subtracting this continuum (bottom panels), detected emission lines are fit with Gaussian functions (blue) to measure fluxes. (Other undetected emission lines are labeled in gray.) The best-fit model continuum is smoothed with a constant spectral resolution (R) of 100, which corresponds to a velocity resolution of $\sim 3000 \text{ km s}^{-1}$. We also see a hint of C IV absorption, as we mention in the last paragraph of Section 3.4. Note that at the wavelength of C IV, $\sim 1-2 \mu\text{m}$, R falls to ~ 30 , which is lower than R in our fitting.

The segmentation process and photometry measurements with the GRIZLI pipeline were done automatically to all detected galaxies in the field with circular apertures. We then measure the photometry of the JD components A and B individually using PIXEDFIT (Abdurrouf et al. 2023) within elliptical apertures as described in Hsiao et al. (2023) centered at the central pixel (brightest pixel in F444W) of each component. Both GRIZLI and PIXEDFIT described in Hsiao et al. (2023) v4 of the images while in this letter we analyze v6 images as described earlier in this section. No significant change is found in the result from the SED fittings. Additionally, we create rectangular photometric apertures that match the NIRSpect slitlets in size, position, and orientation in each of our four observations for JD1 and JD2 (see Figure 1).⁵⁰ We find this photometry is very similar to the photometry of component A, because the NIRSpect slitlets primarily targeted A with

occasional small contributions from the fainter clump B. All resulting NIRCcam photometry is presented in Table 2 and plotted along with the NIRSpect spectrum in Figure 3.

We note the photometry of clump A ($\beta \sim -2.6 \pm 0.1$) is slightly redder than the observed spectrum ($\beta \sim -2.8$). Both measurements present challenges, including the proximity of the A and B clumps, and variable slit loss corrections as a function of wavelength applied by the JWST pipeline to the NIRSpect spectrum.

3. Results and Discussion

We obtain four spectra of MACS0647–JD component A in the lensed images JD1 and JD2 (Figure 1). Obs 21 of JD2 also includes flux from the fainter component B. We have not attempted to extract signal from component B that might be isolated from A in the cross-dispersion direction.

The summed spectrum of all four observations (JD1 Obs 21, JD1 Obs 23, JD2 Obs 21, and JD2 Obs 23) is shown in

⁵⁰ https://github.com/aabdurrouf/JWST-HST_resolvedSEDfits/tree/main/MACS0647-JD

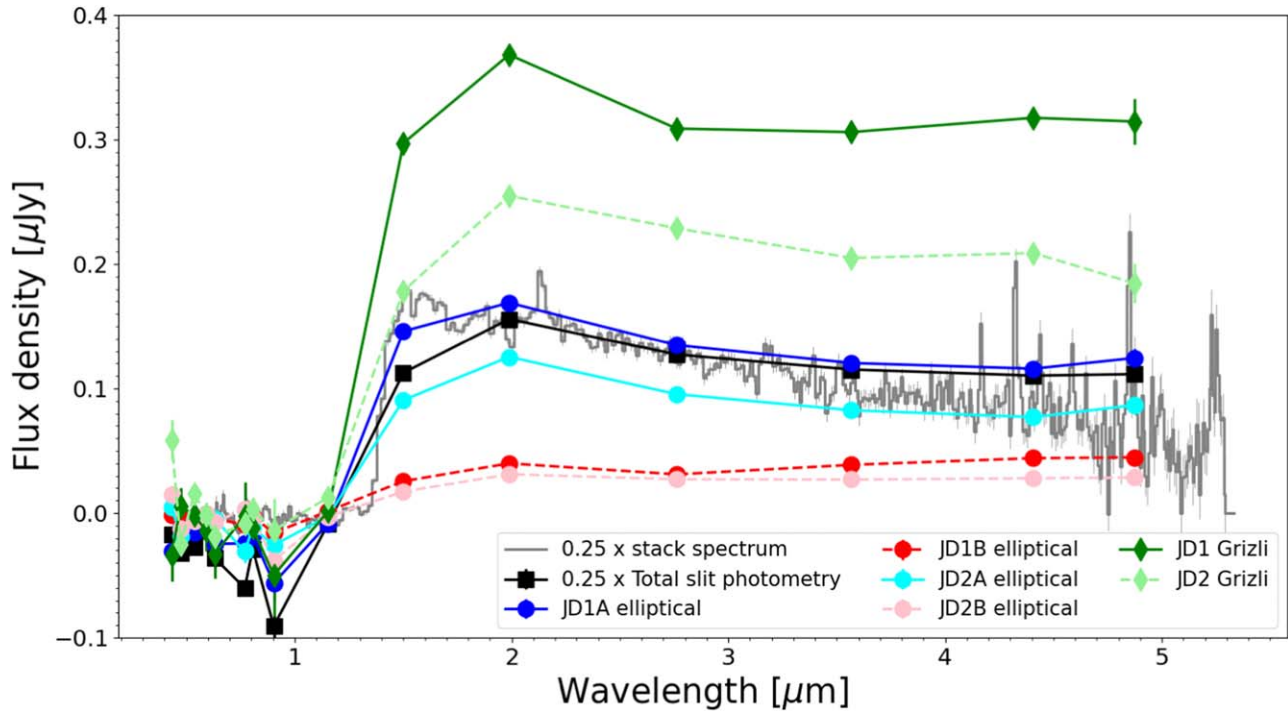


Figure 3. MACS0647–JD NIRSpec summed spectrum (divided by 4; gray) compared with photometry presented in Table 2. Black points show the photometry measured in rectangular apertures that mimic the observed NIRSpec slits. These synthetic colors match the JD1A and JD2A photometry measured within elliptical apertures by PIXEDFIT (blue and cyan, respectively). The smaller clump B is redder (JD1B in red, JD2B in pink). Photometry of the entire galaxy MACS0647–JD lensed images JD1 and JD2 (dark and light green, respectively), including clumps A and B plus additional diffuse light, was measured by GRIZLI with circular apertures of $0''.25$ radius.

Table 2
NIRCam Photometry of MACS0647–JD

Object	Magnif. ^a	Photometry	Aperture	F115W	F150W	F200W	F277W	F356W	F444W	F480M
JD1	~ 8	GRIZLI	circular	1 ± 8	297 ± 7	368 ± 5	309 ± 6	306 ± 6	317 ± 8	314 ± 18
JD2	~ 5.3	GRIZLI	circular	12 ± 7	178 ± 6	255 ± 4	229 ± 5	205 ± 5	209 ± 7	185 ± 16
JD1A	~ 8	PIXEDFIT	elliptical	-8 ± 4	146 ± 3	169 ± 2	135 ± 2	120 ± 2	116 ± 3	124 ± 8
JD2A	~ 5.3	PIXEDFIT	elliptical	-2 ± 3	90 ± 3	125 ± 2	95 ± 2	82 ± 2	77 ± 3	87 ± 7
JD1B	~ 8	PIXEDFIT	elliptical	1 ± 2	26 ± 2	40 ± 2	31 ± 2	39 ± 2	44 ± 2	45 ± 5
JD2B	~ 5.3	PIXEDFIT	elliptical	-3 ± 3	17 ± 2	31 ± 1	27 ± 1	27 ± 1	28 ± 2	29 ± 5
JDA ^b	~ 26.6	PIXEDFIT	rectangular	-35 ± 10	450 ± 8	623 ± 5	509 ± 6	461 ± 6	441 ± 9	446 ± 21

Notes. All flux densities are given in units of nJy, and are not delensed. Photometry is plotted in Figure 3 along with the spectrum.

^a Lensing magnification estimates (Meena et al. 2023).

^b Photometric apertures designed to match the four observed NIRSpec slitlets that primarily observe JDA. Flux densities include the sum of all four.

Figure 2, with a total magnification of $26.6 = 8 + 8 + 5.3 + 5.3$. We detect the continuum between 1.5 and $5.3 \mu\text{m}$ with $S/N > 10$ per spectral resolution element out to $\sim 3 \mu\text{m}$; flux decreases and noise increases to longer wavelengths. Rather than a sharp Lyman break, the spectrum rolls off gradually from $1.5 \mu\text{m}$ (1343 \AA rest frame) to the Lyman break observed at $1.36 \mu\text{m}$ (1216 \AA rest frame). In Section 3.7 we show that this attenuation is consistent with a Ly α damping wing.

We detect seven emission lines (including unresolved doublets): C III] $\lambda\lambda 1907, 1909$, [O II] $\lambda\lambda 3727, 3729$, [Ne III] $\lambda 3869$, [Ne III] $\lambda 3968$, H δ $\lambda 4101$, H γ $\lambda 4340$, and [O III] $\lambda 4363$, all with $S/N > 4$. We also marginally detect He I $\lambda 4473$ with $S/N \sim 2.8$. Based on the observed wavelengths of these lines, we measure a spectroscopic redshift $z_{\text{spec}} = 10.17$. Harikane et al. (2024) recently reported the same redshift for MACS0647–JD based on a fraction of the data: JD1 Obs 23.

The spectroscopic redshift is slightly lower (consistent within 2σ) than the photometric redshifts estimated previously: $z_{\text{phot}} = 10.7^{+0.6}_{-0.4}$ (95% confidence limit) from HST imaging (Coe et al. 2013) and $z_{\text{phot}} = 10.6 \pm 0.3$ from JWST + HST imaging (Hsiao et al. 2023). This may be explained by the Ly α damping wing reducing flux between 1.35 and $1.5 \mu\text{m}$ (in the JWST F150W and HST F140W filters) more than expected for a sharp Lyman break, as assumed in the photometric redshift fitting based on SED modeling.

We measure the emission line fluxes and report them in Table 3. To measure the fluxes, we fit each line with a Gaussian after modeling and subtracting the continuum using PIXEDFIT (Abdurro’uf et al. 2023). The continuum model is fit to the NIRSpec spectrum while masking out the emission lines. The unresolved doublets C III] and [O II] are each fitted with a single Gaussian. Flux uncertainties are estimated using the Monte Carlo method.

Table 3
Measured Emission Line Fluxes for JDA

Emission Lines	Rest Wavelength (Å)	Observed Wavelength (μm)	Line Flux ^a (10^{-20} erg s cm^{-2})	S/N	EW (rest frame; Å)
C III]	1907, 1909	2.13	310 ± 60	5.7	14 ± 3
[O II]	3726, 3729	4.16	42 ± 5	8.9	13 ± 2
[Ne III]	3869	4.32	76 ± 6	13.8	25 ± 2
[Ne III]	3968	4.43	41 ± 6	7.3	15 ± 2
H δ	4101	4.58	40 ± 7	6.1	17 ± 3
H γ	4340	4.85	74 ± 10	7.7	42 ± 6
[O III]	4363	4.87	25 ± 6	4.4	14 ± 3
He I	4473	5.00	24 ± 9	2.8	16 ± 5

Note.

^a As observed in the sum of 4 observations ($=2\mu_{\text{JD1}} + 2\mu_{\text{JD2}} = 2 \times (8 + 5.3)$) divided by 2 with a total magnification ~ 13.3 ($=\mu_{\text{JD1}} + \mu_{\text{JD2}} = 8 + 5.3$), which is not delensed. The equivalent widths (EWs) are shown in the last column.

Recently, Bunker et al. (2023) presented deeper NIRSpectroscopy⁵¹ of GN-z11 at $z = 10.603$ that featured all the lines above, plus additional lines that are not detected in MACS0647–JD: Ly α $\lambda 1216$, N IV] $\lambda 1486$, C IV $\lambda 1549$, He II $\lambda 1640$, N III] $\lambda 1748$, and Mg II $\lambda 2800$. The nitrogen lines N IV] and N III] were surprising detections rarely observed in any galaxy (Cameron et al. 2023a; Charbonnel et al. 2023). The measured line fluxes were $\sim 10^{-18}$ erg s $^{-1}$ cm $^{-2}$. Nitrogen lines that strong would have also been detected in our observations of MACS0647–JD. Note the continuum brightness of GN-z11 is comparable to JD1A (F200W AB mag 25.8 ± 0.1), so similar line fluxes would correspond to similar equivalent widths (EWs; generated by similar physical properties).

3.1. Spectral Modeling

We perform spectrophotometric SED fitting using PIXEDFIT (Abdurro’uf et al. 2021, 2022, 2023). This code fits the spectral continuum (with emission lines masked out) and photometry simultaneously. We use the summed spectrum and the total photometry measured with rectangular apertures resembling the NIRSpectroscopy slits in the four exposures. This code uses Flexible Stellar Population Synthesis (Conroy et al. 2009; Leja et al. 2017) SED models, which have nebular emission incorporated using CLOUDY (Ferland et al. 2017). We assume a Chabrier (2003) initial mass function (IMF), Charlot & Fall (2000) dust attenuation law, and intergalactic absorption based on the Inoue et al. (2014) model. The dust optical depth is denoted $\hat{\tau}_d$. We assume a double power-law SFH with rising slope β , declining slope α , and timescale τ ; star formation rate (SFR) $(t) = [(t/\tau)^\alpha + (t/\tau)^{-\beta}]^{-1}$. Please refer to Abdurro’uf et al. (2023, Table 2 therein) for more information on the definition of these parameters and associated priors.

Gas-phase metallicity Z_{gas} and stellar metallicity Z_* are modeled independently. To reduce the number of free parameters, we fix the ionization parameter $\log(U) = -2.0$ and the gas-phase metallicity Z_{gas} to $12 + \log(\text{O}/\text{H}) = 7.5$ based on our estimate from the emission lines (see Sections 3.6 and 3.5). Varying these values within the uncertainties does not significantly change the results that follow.

First, we use PIXEDFIT to fit the spectral continuum after masking out the emission lines. Then we subtract this best-fit

continuum and fit Gaussians to the emission lines to measure their fluxes and EWs, reported in Table 3.

The spectrum has no Balmer break with $F_{\nu}(4200 \text{ \AA})/F_{\nu}(3500 \text{ \AA}) \sim 0.77 \pm 0.06$, measured as in Binggeli et al. (2019), suggesting a young age. Spectral continuum fitting suggests a very young mass-weighted age of 8_{-2}^{+3} Myr for component A. However, these spectral models do not account for the Ly α damping wing. SED fitting to the photometry (Section 3.2) yields a similarly young age until we omit the F150W flux measurement affected by the Lyman damping. Our measured photometry is also slightly redder than the spectrum, contributing to slightly older age measurements, though still young as we discuss next in Section 3.2.

3.2. Photometric Spectral Energy Distribution Modeling

We perform SED fitting to the NIRCcam photometry of the brightest lensed image JD1 (magnified by $\mu = 8 \pm 1$) for the full galaxy and then for the individual clumps A and B, as reported in Table 2. We exclude the F150W photometry because our spectral models do not include Ly α damping wing. (Including the F150W photometry results in artificially low ages.) We perform SED modeling using three methods: PIXEDFIT (Abdurro’uf et al. 2021; Abdurro’uf et al. 2022; Abdurro’uf et al. 2023), BAGPIPES⁵² (Carnall et al. 2018, 2019), and BEAGLE (Chevallard & Charlot 2016). We describe our methods in Section 3.1 for PIXEDFIT and below for BAGPIPES and BEAGLE. We summarize our results in Table 4.

Our BAGPIPES (Carnall et al. 2018, 2019) method is described in detail in Hsiao et al. (2023). Briefly, we use Binary Population and Stellar Synthesis (BPASS) v2.2.1 templates (Stanway & Eldridge 2018) including binary evolution, with a Kroupa (2001) IMF and upper mass cutoff of $300 M_{\odot}$. Nebular emission is included by processing these stellar models through the photoionization code CLOUDY (Ferland et al. 2017). Dust attenuation is modeled with the Salim et al. (2018) flexible parameterization, including a variable slope and additional dust within star-forming regions < 10 Myr old. Based on our spectroscopic results below, we fix gas metallicity to $Z_{\text{gas}} = 0.1 Z_{\odot}$ and ionization parameter $\log(U) = -2$ (see Section 3.5). Varying these values within their uncertainties does not significantly affect our derived physical parameters.

⁵¹ Exposure times of 6.9 hr with the low-resolution ($R \sim 100$) prism and 3.45 hr in each of three medium resolution ($R \sim 1000$) gratings: G140M/F070LP, G235M/F170LP, and G395M/F290LP.

⁵² <https://bagpipes.readthedocs.io>

Table 4
Physical Properties of JD1, JD1A, and JD1B from Spectral Energy Distribution Fitting Using Various Methods

Component	Code	SFH	Age ^a (Myr)	Stellar Mass $\log(M_*/M_\odot)$	SFR (M_\odot/yr)	sSFR (Gyr^{-1})	Dust (A_V mag)
JD1	BAGPIPES	constant	8_{-2}^{+3}	8.1 ± 0.3	10 ± 3	-7.1 ± 0.3	0.09 ± 0.02
	BAGPIPES	nonparametric	6_{-1}^{+12}	8.0 ± 0.1	10 ± 1	-7.0 ± 0.1	0.09 ± 0.01
	BAGPIPES	delayed τ	3_{-2}^{+3}	$7.7_{-0.1}^{+0.2}$	$5.5_{-1.0}^{+0.8}$	-7.0 ± 0.1	$0.02_{-0.01}^{+0.02}$
	BEAGLE	delayed τ	40_{-25}^{+85}	8.2 ± 0.1	10 ± 1	-7.2 ± 0.1	0.11 ± 0.03
	PIXEDFIT	double power law	30_{-20}^{+53}	8.4 ± 0.3	$4.4_{-1.2}^{+2.5}$	$-7.7_{-0.2}^{+0.1}$	0.05 ± 0.04
JD1A	BAGPIPES	constant	8_{-2}^{+3}	7.6 ± 0.1	3 ± 1	-7.0 ± 0.3	<0.01
	BAGPIPES	delayed τ	5_{-1}^{+2}	7.5 ± 0.1	2.4 ± 0.1	-7.0 ± 0.1	<0.01
	BEAGLE	delayed τ	14_{-3}^{+6}	7.9 ± 0.1	3.3 ± 0.1	-7.3 ± 0.1	0.05 ± 0.01
	PIXEDFIT	double power law	38_{-20}^{+28}	8.1 ± 0.3	1.3 ± 0.6	-8.0 ± 0.1	$0.03_{-0.03}^{+0.04}$
	JD1B	BAGPIPES	delayed τ	50_{-40}^{+60}	7.7 ± 0.3	1.0 ± 0.3	-7.7 ± 0.3
PIXEDFIT		double power law	15_{-10}^{+40}	7.3 ± 0.3	$0.7_{-0.3}^{+0.5}$	$-7.4_{-0.2}^{+0.1}$	0.06 ± 0.04

Notes. The stellar mass and SFR estimates are delensed by a magnification $\mu = 8 \pm 1$ (Meena et al. 2023). Magnification uncertainties are not included in the uncertainties quoted in the table for stellar mass and SFR. Most of these SED fitting methods assume a Chabrier (2003) IMF. BAGPIPES assumes Kroupa et al. (1993); to renormalize those results, we multiplied the stellar masses by 0.94 (Madau & Dickinson 2014). Component JD1 is measured with GRIZLI while JD1A and JD1B are measured using PIXEDFIT (see Table 2). The summed SFR of JD1A and JD1B is of order an order of magnitude lower than the combined JD1, which is likely due to lost fluxes among various apertures (see also Table 2). The seventh column shows the specific SFR (sSFR).

^a Ages are mass-weighted. This equals half the formation age for a constant SFH.

We explore various SFHs: constant, “delayed τ ,” and nonparametric. The delayed τ SFH allows for a linear rise followed by an exponential decline: $\text{SFR}(t) \propto t \exp(-t/\tau)$. Most of our fits only have the linear rise with $\tau > 1$ Gyr. We explore nonparametric SFHs with constant SFR in four time bins (e.g., 0–10–50–150–300 Myr). With these models, we find almost all the SFR ends up in our youngest bin 0–10 Myr, with negligible older populations.

We also use BEAGLE (Chevallard & Charlot 2016) to derive an independent fit to both the photometry and the measured emission line EWs (see Table 3). BEAGLE assumes a Chabrier (2003) IMF and also uses CLOUDY to account for nebular emission. We further assume a delayed τ SFH with an ongoing starburst over the last 10 Myr, an SMC dust attenuation law, and the Inoue et al. (2014) intergalactic medium (IGM) attenuation models. We apply a similar setup and parameter space as in Furtak et al. (2023), though without the external priors and fixing the redshift to the measured spectroscopic value. Here we also leverage the additional information provided by the numerous emission lines to leave the gas-phase metallicity and the dust-to-metal ratio as free parameters. These are modeled with uniform priors $\log(Z_{\text{gas}}/Z_\odot) \in [-2.2, -0.3]$ and $\xi_d \in [0.1, 0.5]$ as in Gutkin et al. (2016) and Chevallard & Charlot (2016).

Based on these various methods, we obtain the results summarized in Table 4. We find MACS0647–JD has a stellar mass $\log(M_*/M_\odot) = 8.1 \pm 0.3$, $\text{SFR} = 10 \pm 3 M_\odot \text{ yr}^{-1}$, and a high sSFR $\sim 80 \text{ Gyr}^{-1}$, where $\text{sSFR} = \text{SFR}/\text{stellar mass}$.

The clump A photometry can be well fit by constant star formation for 17_{-4}^{+5} Myr, corresponding to a mass-weighted age 8_{-2}^{+3} Myr, according to BAGPIPES. Age estimates from the various methods range between 1 and 50 Myr, consistent with the results from Hsiao et al. (2023). We estimate clump A contains about one-third of the stellar mass of MACS0647–JD.

The smaller redder component B photometry is best fit by a linearly rising SFR for 40–300 Myr, with a mass-weighted age of 10–110 Myr, stellar mass $\log(M_*/M_\odot) = 7.9 \pm 0.3$, and dust

$A_V = 0.10 \pm 0.05$ mag. Based on similar age estimates in Hsiao et al. (2023), they suggested clump B may have formed separately and merged with the younger clump A, though different SFHs in situ are also possible.

MACS0647–JD has an absolute UV magnitude $M_{\text{UV}} = -20.3 \pm 0.2$, including $M_{\text{UV}} = -19.5 \pm 0.2$ for clump A and $M_{\text{UV}} = -17.9 \pm 0.2$ for clump B. These are based on the JD1 F200W photometry in Table 2 delensed by a magnification $\mu = 8 \pm 1$.

3.3. Star Formation Rate and History

Hydrogen Balmer line strengths yield robust estimates of recent SFH within the past $\lesssim 10$ Myr. These measurements commonly utilize the strongest Balmer line $H\alpha$ or the second strongest $H\beta$ (e.g., Glazebrook et al. 1999; Erb et al. 2003; Reddy et al. 2008; Madau & Dickinson 2014; Shapley et al. 2023). Both of these are redshifted beyond our observed wavelength range, however we detect both $H\gamma$ and $H\delta$.

Intrinsic Balmer line strength ratios are dictated by atomic physics. For Case B recombination at $T = 10,000$ K, we expect $H\gamma/H\delta = 1.81$ (e.g., Dopita & Sutherland 2003; Groves et al. 2012). In MACS0647–JD, we measure $H\gamma/H\delta \sim 1.88 \pm 0.43$, consistent with expectations ($H\gamma/H\delta = 1.81$) within the uncertainties. Dust reddening may artificially increase observed Balmer line ratios. We cannot place meaningful constraints on the dust extinction, given the large uncertainties in the flux ratio and the similar wavelengths of $H\gamma$ and $H\delta$. Note that Balmer line stellar absorption might affect our measurements of $H\gamma$ and $H\delta$ by 0–5 Å, which are within our uncertainty of 6 Å. We assume no dust, consistent with the result $A_V < 0.02$ mag from SED fitting to the photometry of component A in Hsiao et al. (2023) and similarly in our updated analysis of the latest photometry Section 3.2. Finally, we note the measured $H\gamma$ rest-frame $\text{EW} = 42 \pm 6$ Å may be slightly suppressed by photospheric absorption lines with $\text{EW} < 5$ Å, but that is within our measurement uncertainty.

Table 5
Derived Emission Line Ratios and Expected Values

Line or Line Ratio	Equation/Derivation	Flux or Flux Ratio ^a
H β	2.14 H γ	$(160 \pm 20) \times 10^{-20} \text{ erg s}^{-1} \text{ cm}^{-2}$
H α	6.11 H γ	$(460 \pm 60) \times 10^{-20} \text{ erg s}^{-1} \text{ cm}^{-2}$
Ne3O2	[Ne III] $\lambda 3869$ /[O II] $\lambda 3727$	1.8 ± 0.2
O32	from Ne3O2 ^b ; [O III] $\lambda 5007$ /[O II]	30 ± 6
[O III] $\lambda 5007$	O32 \times [O II]	$(1300 \pm 300) \times 10^{-20} \text{ erg s}^{-1} \text{ cm}^{-2}$
auroral line ratio	[O III] $\lambda 5007$ /[O III] $\lambda 4363$	50 ± 16
[O III] $\lambda \lambda 4959, 5007$	$1.34 \times$ [O III] $\lambda 5007$	$(1700 \pm 400) \times 10^{-20} \text{ erg s}^{-1} \text{ cm}^{-2}$
R23	([O II] + [O III] $\lambda \lambda 4959, 5007$)/H β	11 ± 3

Notes.

^a Measured fluxes in the stacked spectra are magnified by ~ 13.3 .

^b We estimate O32 based on our measured Ne3O2. The two line ratios are strongly correlated at these high values.

Assuming no dust, we estimate the H β and H α line fluxes using the expected line ratios H β = 2.14 H γ and H α = 6.11 H γ (see Table 5). Converting our inferred H α line flux to luminosity, including a deblending correction for magnification, we estimate $L_{\text{H}\alpha} = (4.5 \pm 0.2) \times 10^{41} \text{ erg s}^{-1}$. Adopting an SFR conversion factor of 3.2×10^{-42} suitable for high-redshift galaxies (Reddy et al. 2018), we estimate $\text{SFR} = 1.4 \pm 0.2 M_{\odot} \text{ yr}^{-1}$. Note that the SFR will be higher if there is dust, and the conversion factor is sensitive to the IMF, SFH, and metallicity assuming that the escape fraction is zero (e.g., Wilkins et al. 2019). Also, the SFR derived from the emission lines is smaller than the estimates from the photometry of JD1, but it is consistent with the SFR estimated from the photometry of JD1A. This is likely because the slitlets of four observations mainly targeted JDA (see Figure 1).

Similarly, [O II] $\lambda 3727$ can also be used to estimate the SFR for distant galaxies (e.g., Kennicutt 1998). This yields a slightly lower $\text{SFR}_{\text{O II}} = 0.6 \pm 0.2 M_{\odot} \text{ yr}^{-1}$. However, we note that this empirical calibration was derived for low-redshift galaxies and depends on metallicity and dust, which are lower for high-redshift galaxies like MACS0647–JD.

3.4. Strong C III] $\lambda \lambda 1907, 1909$ Emission

We detect strong emission of C III] $\lambda \lambda 1907, 1909$ (blended) with a line flux of $(3.1 \pm 0.6) \times 10^{-18} \text{ erg s}^{-1} \text{ cm}^{-2}$ and rest-frame $\text{EW} = 14 \pm 3 \text{ \AA}$. Such high EW C III] $\lambda \lambda 1907, 1909$ is associated with low metallicity galaxies experiencing an intense burst of star formation (Rigby et al. 2015); it is predicted for BPASS models (Stanway & Eldridge 2018) only when they include very recent star formation within the past megayear (Jaskot & Ravindranath 2016), consistent with our young age estimates in Section 3.2. We use the measured EW as a metallicity diagnostic in Section 3.6.

We note additional C III] emission appears to come from the B component, which is marginally spatially resolved in the 2D spectrum of JD2 in Obs 21 (Figure 1). This would suggest a young age for B, or at least very recent star formation within the past megayear perhaps in addition to the older star formation and age ($\sim 100 \text{ Myr}$) estimated from the photometry.

Strong C III] emission with high rest-frame EWs of 10–20 \AA or more has been observed in $z \sim 0\text{--}8$ galaxies, often associated with high observed or inferred [O III] + H β EWs $\sim 1000\text{--}2000 \text{ \AA}$ (e.g., Stark et al. 2017; Berg et al. 2019; Hutchison et al. 2019; Mainali et al. 2020; Vanzella et al. 2020; Tang et al. 2021; Mingozzi et al. 2022; Vanzella et al. 2023) or even higher than 2000 \AA (Tang et al. 2023). This is consistent with

our expectation based on our extrapolated [O III] + H β flux (Table 5), which roughly corresponds to an $\text{EW} \sim 1000 \text{ \AA}$, assuming the continuum flux at rest frame $\sim 5000 \text{ \AA}$ is similar to what we measure out to $\sim 4500 \text{ \AA}$.

We do not detect the higher ionization species C IV $\lambda 1549$. This combined with the strong C III] emission suggests that an active galactic nucleus (AGN) is likely not the driving ionizing source in this galaxy. Detections of strong C IV are often associated with AGN activity (e.g., Baskin & Laor 2005; Le Fèvre et al. 2019). However, young stellar populations can also drive strong C IV emission (e.g., Mainali et al. 2017).

If anything, we see a hint of C IV absorption, as also predicted by our PIXEDFIT best-fit model. Such C IV absorption is observed (and modeled) for young stellar populations with ages $< 10 \text{ Myr}$ (e.g., Leitherer et al. 1999; Chisholm et al. 2019) and can constrain stellar age and metallicity when detected at high S/N and resolution. The interstellar medium can also absorb C IV due to internal gas kinematics and/or a high column density (Jaskot & Ravindranath 2016; Steidel et al. 2016).

3.5. Ionization $\log(U)$ and $\log(\xi_{\text{ion}})$

The line ratio O32 = [O III] $\lambda 5007$ /[O II] $\lambda 3727$ has long been used (e.g., Hicks et al. 2002) as a diagnostic for the ionization parameter $\log(U)$. At high redshifts, when [O III] $\lambda 5007$ is unavailable (for example, for galaxies at $z \gtrsim 9.6$, [O III] $\lambda 5007$ shifts beyond the wavelength coverage of 5.3 μm in NIRSspec), the line ratio Ne3O2 = [Ne III] $\lambda 3869$ /[O II] $\lambda 3727$ has been proposed as an alternative diagnostic (Pérez-Montero et al. 2007; Levesque & Richardson 2014; Maiolino & Mannucci 2019; Witstok et al. 2021). Strong correlations are observed between Ne3O2 and O32 in nearby galaxies when all lines are detected with strong significance (Jaskot & Oey 2013; Izotov et al. 2018; Flury et al. 2022), especially the case for higher ionization (i.e., similar to the properties of galaxies expected and found at $z > 6$). More distant galaxies at $z \sim 2\text{--}7$ exhibit similar trends (Christensen et al. 2012; Tang et al. 2019; Vanzella et al. 2020; Tang et al. 2023).

In MACS0647–JD, we measure a high value for Ne3O2 = 1.8 ± 0.2 . According to Witstok et al. (2021, Equations (1)–(3)), this Ne3O2 ratio corresponds to O32 = 30 ± 6 and ionization parameter $\log(U) = -1.84 \pm 0.06$, using $\log(U) = 0.80 \times \log(\text{O32}) - 3.02$ from Díaz et al. (2000).

We also used HII-CHI-MISTRY version 5.22⁵³ (Pérez-Montero 2014) to estimate $\log(U)$ using the observed and

⁵³ <https://home.iaa.csic.es/~epm/HII-CHI-mistry-opt.html>

Table 6
Metallicity Estimates

Method	Emission Line(s)	$12 + \log(\text{O}/\text{H})$	Z
PYNEB	[O II], [O III] $\lambda 4363$; extrapolated ^a $\text{H}\beta$, [O III] $\lambda 5007$	8.0 ± 0.2	$0.20_{-0.07}^{+0.12} Z_{\odot}$
HII-CHI-MISTRY	[O II], [Ne III] $\lambda 3869$, [O III] $\lambda 4363$; extrapolated ^a $\text{H}\beta$	7.5 ± 0.2	$0.06_{-0.02}^{+0.04} Z_{\odot}$
Ne3O2	[O II], [Ne III] $\lambda 3869$	7.6 ± 0.3	$0.08_{-0.04}^{+0.08} Z_{\odot}$
R23	[O II]; extrapolated ^a $\text{H}\beta$, [O III] $\lambda 5007$	8.0 ± 0.3	$0.20_{-0.10}^{+0.20} Z_{\odot}$
R23 and O32	[O II]; extrapolated ^a $\text{H}\beta$, [O III] $\lambda 5007$	7.7 ± 0.2	$0.10_{-0.04}^{+0.06} Z_{\odot}$
EW(C III)	C III]	7.8 ± 0.2	$0.13_{-0.05}^{+0.07} Z_{\odot}$

Note.

^a Extrapolated line fluxes correspond to those derived from either the theoretical line ratios (e.g., $\text{H}\beta/\text{H}\gamma$) or empirical calibrations (e.g., Ne3O2 vs. O3O2).

Table 7

Physical Properties of MACS0647–JD (Entire Galaxy) and Individual Clumps A and B, Estimated Based on Observed and Estimated Line Fluxes and Spectral Energy Distribution Fitting to the Photometry

Parameter	Variable	MACS0647–JD	Clump A	Clump B
Emission Lines				
Metallicity (gas phase)	$12 + \log(\text{O}/\text{H})$		7.5–8.0	
	Z_{gas}/Z_{\odot}		0.06–0.2	
Ionization parameter	$\log(U)$		-1.9 ± 0.2	
Ionizing photon production efficiency	$\log(\xi_{\text{ion}}/\text{erg}^{-1} \text{ Hz})$		25.2 ± 0.2	
SFR	$\text{SFR} (M_{\odot} \text{ yr}^{-1})$		1.4 ± 0.2	
SED Fitting				
Absolute UV magnitude	M_{UV} (AB mag)	-20.3 ± 0.2	-19.5 ± 0.2	-17.9 ± 0.2
SFR	$\text{SFR} (M_{\odot} \text{ yr}^{-1})$	8 ± 3	2 ± 1	0.9 ± 0.3
Stellar mass	$\log(M_{*}/M_{\odot})$	8.1 ± 0.3	7.8 ± 0.3	7.5 ± 0.3
sSFR	$\log(\text{sSFR}/\text{Gyr}^{-1})$	-7.1 ± 0.3	-7.2 ± 0.3	-7.5 ± 0.3
Mass-weighted age	age_{M} (Myr)	20 ± 20	10_{-9}^{+30}	40 ± 30
Dust	A_{V} (mag)	0.07 ± 0.06	< 0.06	0.10 ± 0.05

Notes. The SFR (average within the past 10 Myr) and stellar mass are corrected for lensing magnification. BAGPIPES assumes Kroupa et al. (1993); to renormalize those results, we multiplied the stellar masses by 0.94 (Madau & Dickinson 2014).

extrapolated line flux ratios discussed in Section 3.6 and listed in Table 6. Our inputs were measured line fluxes for [O II] $\lambda 3727$, [Ne III] $\lambda 3869$, and [O III] $\lambda 4363$, all normalized to our extrapolated $\text{H}\beta$ flux based on $\text{H}\gamma$. Here we did not use the extrapolated [O III] $\lambda 5007$ flux. We obtain an ionization parameter of $\log(U) = -2.09 \pm 0.02$, similar to but slightly lower than the value estimated above from Ne3O2.

Kewley et al. (2019) noted the line ratio C III] $\lambda \lambda 1907, 1909$ /[C II] $\lambda 2325$ (blend) could be an excellent diagnostic for ionization parameter $\log(U)$ at low metallicities $12 + \log(\text{O}/\text{H}) < 8.5$ (see their Figure 7). Our nondetection of [C II] with flux $< 0.55 \times 10^{-18} \text{ erg s}^{-1} \text{ cm}^{-2}$ (1σ limit), yielding a line ratio C III]/[C II] > 5.7 , corresponds to $\log(U) > -2.8$ for $12 + \log(\text{O}/\text{H}) \sim 7.6$.

We conclude $\log(U) = -1.9 \pm 0.2$ based on the three estimates (see also Table 7). This is comparable to the value $\log(U) \sim -2$ obtained for GN-z11 (Bunker et al. 2023).

Our $\text{H}\alpha$ luminosity measurement (delensed and assuming no dust) yields an estimate for the production rate of hydrogen-ionizing photons: $\dot{N}_{\text{ion}} = (3.3 \pm 0.1) \times 10^{53} \text{ s}^{-1}$ ($\log(L_{\text{H}\alpha}) = \log(\dot{N}_{\text{ion}}/s) - 11.87$). Assuming the escape fraction is zero, combined with our measured and demagnified UV luminosity for clump A (corresponding to $M_{\text{UV}} = -19.5 \pm 0.2$), we estimate an ionizing photon production efficiency $\xi_{\text{ion}} = \dot{N}_{\text{ion}}/L_{\nu}^{\text{UV}} = 1.6 \pm 0.3 \times 10^{25} \text{ erg}^{-1} \text{ Hz}$, or $\log(\xi_{\text{ion}}) =$

25.2 ± 0.2 . This is consistent with predictions for high-redshift galaxies ($z > 8$), with higher values expected for younger ($\lesssim 10^8 \text{ yr}$), lower-metallicity galaxies ($Z \lesssim Z_{\odot}$; e.g., Schaerer 2003; Robertson et al. 2013; Wilkins et al. 2016). Observationally, recent JWST studies reported higher values $\log(\xi_{\text{ion}}) \sim 25.7 - 26.0 \text{ erg}^{-1} \text{ Hz}$ for high-redshift ($7 < z < 11$) galaxies (e.g., Bunker et al. 2023; Fujimoto et al. 2023; Tang et al. 2023). Our \dot{N}_{ion} estimate should be treated as a lower limit that could increase due to dust and/or escape fraction f_{esc} .

3.6. Metallicity

We use various methods and line ratio diagnostics to estimate MACS0647–JD’s gas-phase metallicity $12 + \log(\text{O}/\text{H}) = 7.5\text{--}8.0$, or $(0.06\text{--}0.2) Z_{\odot}$, where we adopt a solar metallicity $12 + \log(\text{O}/\text{H}) = 8.69$ (Asplund et al. 2021). Table 6 summarizes our results, and we describe our methods below.

The auroral line [O III] $\lambda 4363$ can provide a “direct” metallicity measurement via the electron temperature when detected and measured along with other lines including [O III] $\lambda \lambda 4959, 5007$ (e.g., Peimbert 1967; Osterbrock 1989; Sanders et al. 2024). Given our estimate O32 = 30 ± 6 (Section 3.5) and observed line flux for [O II], we can estimate the expected [O III] $\lambda 5007$ line flux as $(1.3 \pm 0.3) \times 10^{-17} \text{ erg s}^{-1} \text{ cm}^{-2}$,

assuming no dust, or ~ 50 times stronger than [O III] $\lambda 4363$. Note the [O III] $\lambda 5007$ line is 2.98 times stronger than [O III] $\lambda 4959$ (Storey & Zeppen 2000), so our extrapolated combined [O III] $\lambda\lambda 4959, 5007$ flux is 1.34 times the [O III] $\lambda 5007$ flux.

We use PYNEB (Luridiana et al. 2015) to analyze the observed and extrapolated emission line ratios. For the entire procedure, we assumed no dust and an electron density $n_e = 100 \text{ cm}^{-3}$. First, we use the task `getCrossTemDen`, taking into account the [O III] $\lambda 5007/\lambda 4363 \sim 50$ with a 20% uncertainty. In this way, we obtain the electron temperature of the high-ionization zone $T_e(\text{[O III]}) = 15,000 \pm 1400 \text{ K}$. The T_e uncertainty is estimated by running the task 1000 times and taking the standard deviation of all the values. Then, we use the Garnett (1989) relation to estimate the low-ionization gas temperature $T_e(\text{[N II]}) = 13,600 \pm 1000 \text{ K}$. Finally, we calculated the O^{++} and O^+ ionic abundances with the task `getCrossTemDen`, using as input [O III] $\lambda 5007/\text{H}\beta \sim 8$ and $T_e(\text{[O III]})$, and [O II] $\lambda 3727/\text{H}\beta \sim 0.26$ and $T_e(\text{[N II]})$, respectively, with the same method to estimate the uncertainties. The total of both species yields $12 + \log(\text{O}/\text{H}) = 8.0 \pm 0.2$, or $\sim 20\% Z_\odot$ ($0.13\text{--}0.32 Z_\odot$).

We also utilize HII-CHI-MISTRY version 5.22 to analyze our observed line ratios, as described in Section 3.5. We obtain $12 + \log(\text{O}/\text{H}) \sim 7.5 \pm 0.2$, corresponding to $\sim 0.06_{-0.02}^{+0.04} Z_\odot$.

Next, we turn to line ratio diagnostics, beginning with Ne3O2. Previous reviews find no strong correlation between Ne3O2 and metallicity, as seen, for example, in local metal-poor galaxies ($Z < 0.6 Z_\odot$) analyzed by Nakajima et al. (2022, Figure 9 therein). But the few galaxies with high Ne3O2 ~ 2 in that study were clustered between roughly $12 + \log(\text{O}/\text{H}) = 7.6 \pm 0.2$, or $0.05\text{--}0.13 Z_\odot$. It is unclear if that low-redshift result ($z < 0.1$) can be extended to high-redshift galaxies.

Another metallicity diagnostic is the line ratio R23 = ([O III] $\lambda\lambda 4959, 5007 + \text{[O II] } \lambda 3727)/\text{H}\beta$ (e.g., Nakajima et al. 2022; Sanders et al. 2024). Based on our observed [O II], extrapolated [O III], and $\text{H}\beta$ inferred from $\text{H}\gamma$, we extrapolate $\text{R23} = 11 \pm 3$. This is among the highest values measured for local metal-poor galaxies by Nakajima et al. (2022). That puts $\text{R23} \sim 11$ in the zone of confusion in the bimodal R23–metallicity relation, severely limiting its usefulness as a metallicity diagnostic, though it can still provide a rough estimate. We note in Nakajima et al. (2022, Figure 3), that galaxies with $\text{R23} = 11 \pm 3$ have metallicities $12 + \log(\text{O}/\text{H}) = 8.0 \pm 0.3$, or between ~ 0.1 and $0.4 Z_\odot$. We note some of the scatter in the R23 versus Z is due to ionization, with higher ionization yielding higher R23 values for a fixed metallicity (e.g., Pérez-Montero 2014, Figure 5).

Izotov et al. (2021) propose a metallicity indicator combining R23 and O32 (their Equation (5)) for improved accuracy at low metallicities $< 6\% Z_\odot$, or $12 + \log(\text{O}/\text{H}) < 7.5$. Nakajima et al. (2023) show this relation works up to $12 + \log(\text{O}/\text{H}) \sim 7.8$ for $z = 4\text{--}8.5$ galaxies with direct metallicity measurements from NIRSPEC. For MACS0647–JD, this relation yields $12 + \log(\text{O}/\text{H}) \sim 7.7 \pm 0.2$, or $0.06\text{--}0.16 Z_\odot$.

Finally, we use the rest-frame UV line C III] $\lambda\lambda 1907, 1909$ as a metallicity diagnostic. Mingozzi et al. (2022) analyzed 45 local ($z < 0.2$) high-redshift analogs observed by the CLASSY survey (Berg et al. 2022), measuring a relation between C III] EW and metallicity with 0.18 dex intrinsic scatter for galaxies with $\text{EW} > 5 \text{ \AA}$. Using their Equation (7) and our observed

C III] EW of $14.2 \pm 2.5 \text{ \AA}$ (discussed in Section 3.4), we estimate $12 + \log(\text{O}/\text{H}) = 7.84 \pm 0.18$, or $0.09\text{--}0.21 Z_\odot$.

We find broad general agreement among our six metallicity indicators with best-fit estimates ranging between $12 + \log(\text{O}/\text{H}) = 7.5\text{--}8.0$, or $(0.06\text{--}0.2) Z_\odot$, as summarized in Table 6, which is also consistent with the metallicity of $12 + \log(\text{O}/\text{H}) = 7\text{--}7.8$ expected from Astraeus simulations for galaxies at $z \sim 10$ with a stellar mass of $10^{8.1} M_\odot$ (Ucci et al. 2023). This is promising for future studies that only have one or more of these diagnostics available either in the rest-frame optical or rest-frame UV. On the other hand, greater precision will be achieved by generally improving these diagnostics and in our specific case by obtaining additional spectra of MACS0647–JD covering longer wavelengths including [O III] $\lambda\lambda 4959, 5007$, $\text{H}\beta$, and $\text{H}\alpha$.

3.7. Ly α Damping Wing

The Ly α photon scattering cross section as a function of wavelength is given by the Voigt profile, which combines a Gaussian core and Lorentzian wings (Tasitsiomi 2006). Resonant scattering of Ly α photons by the neutral IGM suppresses line and continuum fluxes at wavelengths bluer than the rest-frame Ly α at 1216 \AA . Additionally, the Lorentzian wing cross section contributes attenuation to the redward continuum, softening the shape of the Ly α break. This is known as Ly α damping wing attenuation (Miralda-Escudé 1998). Features like these have been observed in quasars (e.g., Mortlock et al. 2011; Bañados et al. 2018; Davies et al. 2018; Wang et al. 2020; Yang et al. 2020), and they have been utilized to investigate not only the average neutral fraction but also specific regions along different sight lines in the IGM at $z > 7$. Recently, this effect has been observed in NIRSPEC prism observations of high-redshift galaxies ($z > 8$; Arrabal Haro et al. 2023a, 2023b; Bunker et al. 2023; Curtis-Lake et al. 2023; Boyett et al. 2024).

We model the Ly α damping wing optical depth following Equation (30) in Dijkstra (2014), as done in Arrabal Haro et al. (2023a, 2023b). The Ly α damping wing description has two free parameters (with redshift held fixed at our measured $z = 10.17$): (1) the neutral hydrogen fraction in the IGM ($X_{\text{H I}}$) and (2) the size of the ionized bubble ($R_{\text{H II}}$), or Stromgren sphere. In short, a higher neutral fraction in the IGM makes the break cutoff become smoother, and a larger ionized bubble size shifts the break blueward allowing the escape of photons at wavelengths shorter than the rest-frame Ly α . To reproduce the observed continuum spectrum, the galaxy model SEDs are convolved with the IGM transmission ($T_{\text{IGM}} \propto e^{-\tau}$, where τ is the damping wing optical depth). We then smooth the model spectra with prism spectral resolution and apply an additional 5% of systemic errors in the χ^2 estimation.

We perform fitting using the Markov Chain Monte Carlo (MCMC) sampler package described in Jung et al. (2017). We use flat linear priors for the free parameters $X_{\text{H I}}$ and $R_{\text{H II}}$. In each MCMC chain step, we take a random model spectrum from the range of models generated by PIXEDFIT (see Section 3.2) to accommodate the uncertainties in the galaxy SED modeling. The wavelength range of the spectrum fitted by PIXEDFIT is between 1.5 and $5.2 \mu\text{m}$ and the fitting does not include modeling of the absorption by damped Ly α (DLA). The inclusion of the additional attenuation by an immediate DLA can reproduce the observed spectra well as in Heintz et al. (2024).

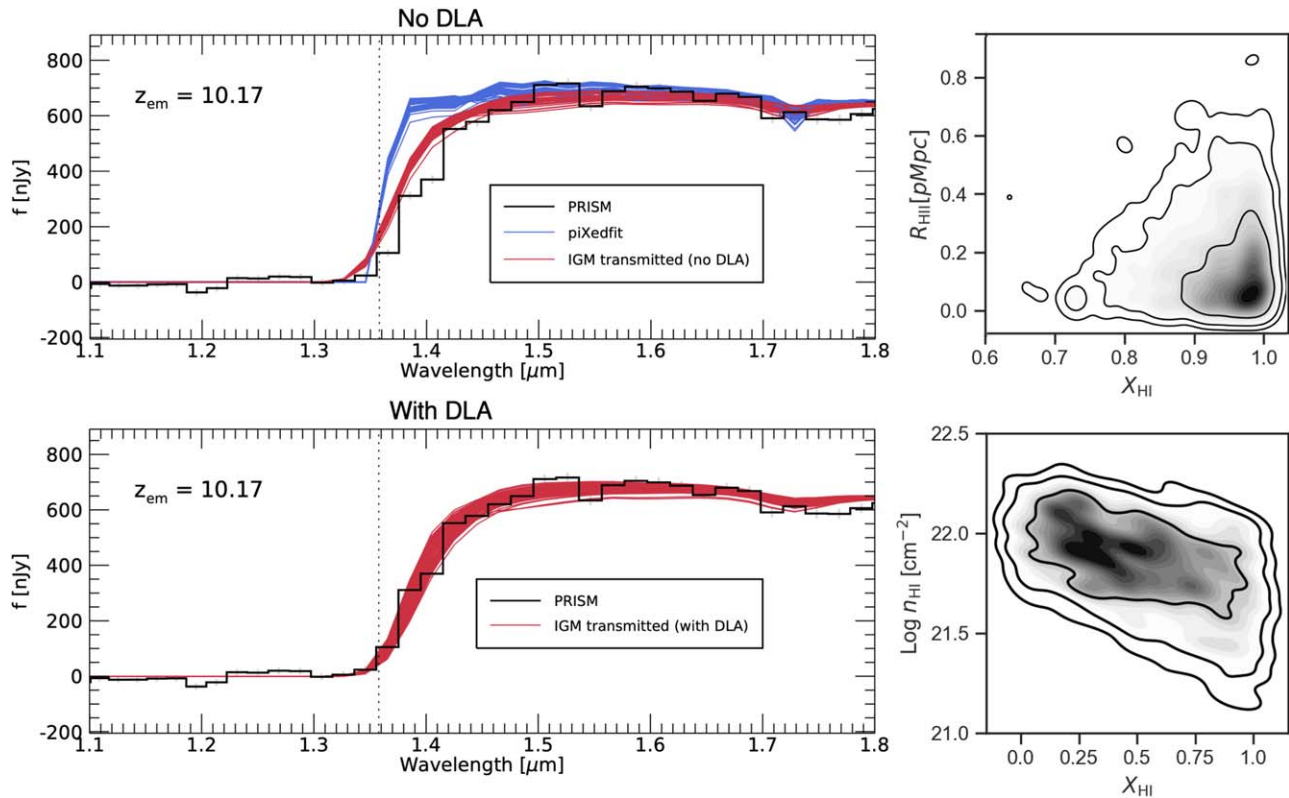


Figure 4. Top: Ly α damping wing analysis of MACS0647–JD without a DLA contribution. The left panel shows the PIXEDFIT SED model (blue) convolved with the IGM transmission and NIRSPEC prism spectral resolution, resulting in the transmitted model spectrum (red). The vertical dotted line denotes the systemic wavelength of Ly α at $z = 10.17$. The right panel displays 1σ , 2σ , and 3σ contours of the probability distributions of $X_{\text{H I}}$ and $R_{\text{H II}}$. The best fit suggests a highly neutral IGM ($X_{\text{H I}} > 0.9$ at a 1σ lower limit) with a small ($R_{\text{H II}} < 0.2$ pMpc) ionized bubble around MACS0647–JD, although the modeled spectra show a still considerably steeper break than observed (black). Bottom: Ly α damping wing analysis with a DLA system. The inclusion of a DLA contribution better reproduces the observed Ly α break shape (left panel). However, the H I column density of the DLA ($n_{\text{H I}}$) is highly degenerate with the neutral IGM fraction, making it highly unconstrained.

Figure 4 shows our results suggesting a small-sized ionized bubble ($R_{\text{H II}} \ll 1$ pMpc) with a highly neutral IGM ($X_{\text{H I}} > 0.9$ at a 1σ lower limit). We experiment with different priors on $X_{\text{H I}}$, including simply assuming a completely neutral IGM ($X_{\text{H I}} = 1$) as inferred from other works (e.g., Barkana & Loeb 2001; Treu et al. 2013; Mason et al. 2018; Bruton et al. 2023), and a logarithmic prior. These priors do not significantly affect our bubble size estimates.

The $R_{\text{H II}}$ estimate appears reliable in the sense that the observed spectra show no positive signals blueward of the systemic wavelength of Ly α . However, the interpretation of the $X_{\text{H I}}$ measurement is rather complicated. The modeled spectra present a Ly α break still considerably steeper than the observed spectrum. As the modeled spectra already include Ly α damping wing opacity with an almost fully neutral IGM, such discrepancies cannot be explained with the IGM attenuation alone. In fact, the total Ly α optical depth combines the IGM damping wing optical depth (τ_{IGM}) and the optical depth due to resonant scattering within the circumgalactic medium (CGM; Dijkstra 2014). However, the latter part is missed in our simple description of the damping wing opacity. To mitigate the differences between the modeled spectra and the observed, it is necessary to carefully model the CGM contribution (Sadoun et al. 2017; Weinberger et al. 2018; Mason & Gronke 2020). Including the CGM contribution would result in additional softening of the Ly α break closer to the observed spectrum, which possibly requires less contribution from IGM attenuation and could allow for a slightly more ionized IGM.

We attempt to model the spectra with a DLA system, following the approach in Heintz et al. (2024). The results with the DLA contribution are shown at the bottom of Figure 4. The inclusion of a DLA better reproduces the observed spectrum, with a DLA H I column density of $\log(n_{\text{H I}}, \text{cm}^{-2}) = 21.9 \pm 0.2$, comparable to Heintz et al. (2024). This analysis reveals that the IGM damping wing attenuation is highly degenerate with the effect of DLA systems. Consequently, including DLAs makes the neutral hydrogen fraction highly unconstrained (bottom right in Figure 4). However, this improved fit underscores the complexity of disentangling the contributions from DLAs and the IGM in such high-redshift observations. However, detailed modeling of Ly α attenuation of the CGM requires knowledge of the density profiles of H I gas and radiation field from a host galaxy (Weinberger et al. 2018; Mason & Gronke 2020), which is beyond the scope of this study. Also, the relation between IGM attenuation and bubble size can deviate from the theoretical model of Dijkstra (2014) due to the stochasticity of individual sight lines, such as fluctuations in density or velocity and random encounters of self-shielded systems (Hutter et al. 2014; Park et al. 2021; Smith et al. 2022). Ideally, one needs to average over a large number of observations to suppress such uncertainties. Additionally, the uncertainties in modeling intrinsic rest-frame UV spectra make the interpretation more complicated.

3.8. Ionized Bubble Size

We also estimate the radius of the ionized bubble around MACS0647–JD by integrating the total ionizing photon

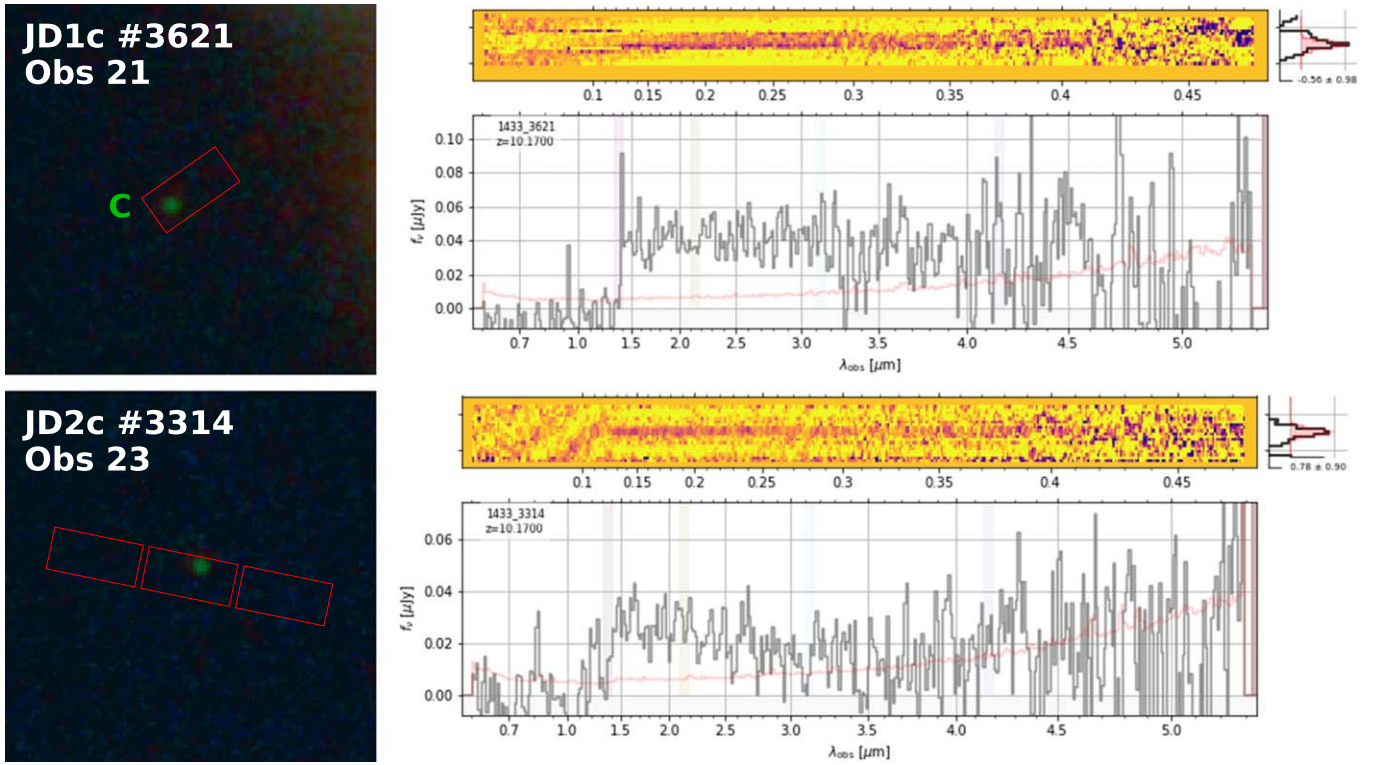


Figure 5. NIRSpec prism spectra of two lensed images of the candidate companion galaxy C. The panels show the slitlet coverage, 2D spectra, and 1D extractions, similar to Figure 1 for MACS0647–JD. Redshift is fixed to the same value $z = 10.17$.

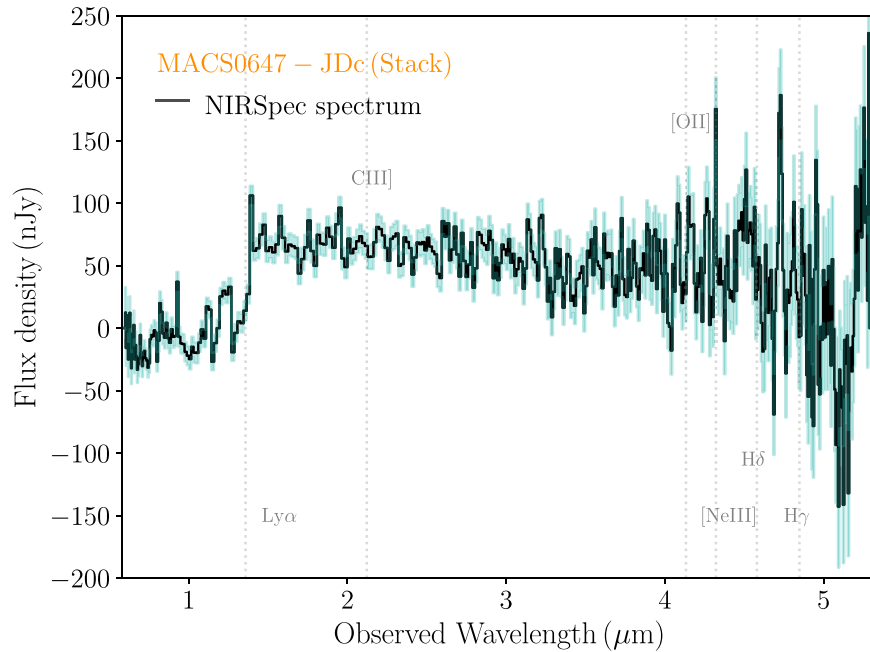


Figure 6. Sum of the spectra shown in Figure 5 for two lensed images of the candidate companion galaxy C. No emission lines are confidently detected; their expected wavelengths are labeled assuming a redshift $z = 10.17$ as derived for MACS0647–JD.

production over the galaxy’s lifetime as in Shapiro & Giroux (1987):

$$\frac{4}{3}\pi R_{\text{HII}}^3 \sim \frac{\dot{N}_{\text{ion}} f_{\text{esc}} t_*}{X_{\text{HI}} n_{\text{H}}}. \quad (1)$$

We estimate $\dot{N}_{\text{ion}} \sim 3.3 \times 10^{53} \text{ s}^{-1}$ based on $\text{SFR} \sim 1.4 M_{\odot} \text{ yr}^{-1}$ for clump A (Section 3.5) with stars having formed

continuously for perhaps $t_* \sim 20 \text{ Myr}$ (Section 3.2). The average density of hydrogen particles in the universe at $z = 10.17$ is $n_{\text{H}} \sim 7 \times 10^{69} \text{ Mpc}^{-3}$, where $n_{\text{H}} = (1 - Y_{\text{He}})\rho_{\text{crit}} \Omega_{\text{b}}(1 + z)^3 m_{\text{H}}^{-1}$. And here we assume a neutral IGM ($X_{\text{HI}} = 1$).

We do not estimate f_{esc} for MACS0647–JD in this work. Here, it suffices to explore possible values. For example, $f_{\text{esc}} = 10\%$ yields $R_{\text{HII}} \sim 0.09 \text{ pMpc}$. A more extreme $f_{\text{esc}} = 50\%$ would only increase that to $R_{\text{HII}} \sim 0.15 \text{ pMpc}$.

Above, we use the SFR for clump A. The entire galaxy has $\text{SFR} \sim 10 M_{\odot} \text{ yr}^{-1}$, or $\sim 7\times$ higher. We might expect that most of the ionizing radiation comes from the blue clump A. But even generously assuming the same ionizing photon production efficiency ξ_{ion} for the entire galaxy and increasing N_{ion} by $4\times$, $R_{\text{H II}}$ only increases by a factor of ~ 1.6 to $R_{\text{H II}} \sim 0.24 \text{ pMpc}$, again assuming a very high $f_{\text{esc}} = 50\%$.

We note these are only rough estimates subject to significant uncertainties. Dense neutral gas clouds in the IGM may impede expansion of the reionized bubble. Some of the reionized gas may recombine, further reducing the bubble size, especially if the ionizing flux wavers due to variations in SFR or f_{esc} .

On the other hand, the total ionizing flux might be much stronger than we have estimated here due to fainter undetected companions, especially given that MACS0647–JD is a merger.

3.9. Candidate Companion Galaxy C

As discovered in Hsiao et al. (2023), a nearby triply lensed J -band dropout galaxy is suspected to be a companion of MACS0647–JD $\sim 3 \text{ kpc}$ away. The photometric redshift and geometric lens model redshift of this companion ‘‘C’’ are consistent with MACS0647–JD of 10.17; the observed lensed positions require a similar or identical redshift. Here we show the NIRSpec spectra of the candidate companion C in Figure 5 and the 1D sum in Figure 6. The Obs 21 spectrum shows a clear Lyman break consistent with $z = 10.17$. The Obs 23 spectrum is noisier but also consistent with the redshift of MACS0647–JD ($z = 10.17$). This supports our conclusion from Hsiao et al. (2023) that MACS0647–JD is likely the most distant galaxy merger known at $z = 10.17$, including two merging components A and B plus a third component C nearby, where component C may indeed be a companion of A and B components.

Given the lower S/N spectrum of companion C, we do not detect emission lines, nor do we detect the $\text{Ly}\alpha$ damping wing expected due to the proximity to A.

4. Conclusions

In this study, we report NIRSpec prism observations of MACS0647–JD, primarily targeting its small component A with de lensed radius $r \sim 70 \text{ pc}$. We measure a spectroscopic redshift $z = 10.17$ based on detections of seven emission lines: C III] $\lambda\lambda 1907, 1909$, [O II] $\lambda 3727$, [Ne III] $\lambda 3869$, [Ne III] $\lambda 3968$, H δ , H γ , and [O III] $\lambda 4363$.

This redshift is slightly lower than the photometric redshift $z \sim 10.6$ estimated previously based on HST and JWST + HST imaging. This may be explained by a $\text{Ly}\alpha$ damping wing revealed by NIRSpec that suppresses the photometry at $\sim 1.5 \mu\text{m}$ more than expected for a sharp Lyman break. Based on observed and extrapolated line ratios of JDA, we estimate an ionization parameter $\log(U) = -1.9 \pm 0.2$, and ionizing photon production efficiency $\log(\xi_{\text{ion}}) = 25.2 \pm 0.2$ for clump A. This $\log(\xi_{\text{ion}})$ value is similar to values measured in sub- L^* $z \sim 4\text{--}5$ galaxies (Bouwens et al. 2016) but lower than measured in $z \sim 7\text{--}8$ galaxies: $\log(\xi_{\text{ion}}) = 25.7\text{--}26.0$ (Tang et al. 2023).

Based on the observed and extrapolated line ratios of JDA, we also estimate a gas-phase metallicity $12 + \log(\text{O}/\text{H}) = 7.5\text{--}8.0$, or $(0.06\text{--}0.2) Z_{\odot}$ derived using six different methods, including optical line diagnostics as well as one diagnostic based on the rest-frame UV line C III] (Mingozzi et al. 2022). The derived metallicities are consistent across the

different methods. The overall agreement is encouraging, supporting the use of each individual method in galaxies with fewer detected emission lines. Additional MIRI spectroscopy covering [O III] $\lambda\lambda 4959, 5007$, H β , and H α would enable a more precise ‘‘direct’’ metallicity measurement when combined with the other lines presented here, including the auroral line [O III] $\lambda 4363$.

The total stellar mass of MACS0647–JD is $\log(M/M_{*}) = 8.1 \pm 0.3$ based on SED fitting to the photometry of the entire galaxy including both clumps A and B. This is toward the low end of stellar masses for $z = 4\text{--}10$ galaxies with direct metallicity estimates from JWST NIRSpec spectroscopy (Nakajima et al. 2023). The metallicity of MACS0647–JD at $z = 10.17$ (if we assume the metallicity of clump A is representative of the whole galaxy) is consistent with the metallicities measured for $4 < z < 10$ galaxies of similar stellar mass.

MACS0647–JD has a de lensed absolute UV magnitude $M_{\text{UV}} = -20.3 \pm 0.2$, including $M_{\text{UV}} = -19.5 \pm 0.2$ for clump A and $M_{\text{UV}} = -17.9 \pm 0.2$ for clump B. SED fitting to the observed photometry of clump A yields a stellar mass $\log(M/M_{*}) = 7.8 \pm 0.3$, likely all produced within the most recent 20 Myr. This young age estimate is supported by the observed strong C III] $\lambda\lambda 1907, 1909$ with rest-frame $\text{EW} = 14 \pm 2 \text{ \AA}$. The SFR of clump A based on H γ and assuming no dust is $1.4 \pm 0.2 M_{\odot} \text{ yr}^{-1}$ over the past 10 Myr. This is similar to the estimate $2 \pm 1 M_{\odot} \text{ yr}^{-1}$ based on SED fitting to clump A’s photometry.

Clump B is likely older with a rising SFH over $\sim 50 \text{ Myr}$ or more, stellar mass $\log(M/M_{*}) = 7.8 \pm 0.3$, and $0.13 \pm 0.07 \text{ mag}$ of dust. The older age of clump B suggests it may have merged with clump A rather than the two clumps forming together in the same galaxy (Hsiao et al. 2023). Spectroscopy of a nearby galaxy C $\sim 3 \text{ kpc}$ away (de lensed) reveals a Lyman break consistent with MACS0647–JD’s redshift $z = 10.17$. This companion C may be destined to merge with A and B. MACS0647–JD is likely the most distant galaxy merger yet known.

Emission line spectroscopy is possible for the triply lensed galaxy MACS0647–JD thanks to its three images magnified by factors $\sim 8, 5$, and 2. The brightest lensed image JD1 is F200W AB mag 25.0 ± 0.1 , including AB mag 25.8 ± 0.1 for clump A. Of all known $z > 10$ galaxies, only GN-z11 at $z = 10.603$ (Bunker et al. 2023) is similarly bright (F200W AB mag 26.0 ± 0.1 ; Tacchella et al. 2023), while most others are AB mag 28–29 (Arrabal Haro et al. 2023a; Curtis-Lake et al. 2023). MACS0647–JD and GN-z11 offer unique opportunities for detailed studies of galaxies within the first 500 Myr.

Many of the physical properties presented in this work rely on extrapolations for [O III] $\lambda 5007$, H β , and/or H α line fluxes. With our granted JWST time in Cycle 2, we will obtain MIRI MRS spectroscopy covering $\sim 5\text{--}7.7 \mu\text{m}$ of observed wavelength (rest frame of $0.45\text{--}0.7 \mu\text{m}$), which will reveal those emission lines (though H β is likely too faint for detection) and enable a more robust analysis of this galaxy. The observation will give spatially resolved spectra that cover both clumps A and B as well as component C of the JD1 system, which gives an opportunity to further confirm the merging nature of this system. In addition to this, we will also obtain high-resolution NIRSpec spectroscopy to better resolve the emission lines currently detected in our prism spectrum, enabling a better measurement of the EW.

Acknowledgments

We thank the anonymous referee for useful comments and constructive remarks on the manuscript.

We are grateful and indebted to the 20,000 people who worked to make JWST an incredible discovery machine.

This work is based on observations made with the NASA/ESA/CSA James Webb Space Telescope (JWST) and Hubble Space Telescope (HST). The data were obtained from the Mikulski Archive for Space Telescopes (MAST) at the Space Telescope Science Institute (STScI), which is operated by the Association of Universities for Research in Astronomy (AURA), Inc., under NASA contract NAS 5-03127 for JWST.

These observations are associated with programs JWST GO 1433 and HST GO 9722, 10493, 10793, and 12101.

T.H. and A. were funded by a grant for JWST GO-01433 and JWST-GO-04212 provided by STScI under NASA contract NAS 5-03127. A.A. acknowledges support from the Swedish Research Council (Vetenskapsrådet project grants 2021-05559). P.D. acknowledges support from the NWO grant 016.VIDI.189.162 (“ODIN”) and the European Commission’s and University of Groningen’s CO-FUND Rosalind Franklin program. The Cosmic Dawn Center is funded by the Danish National Research Foundation (DNRF) under grant #140. E.Z. and A.V. acknowledge support from the Swedish National Space Agency. E.Z. also acknowledges grant 2022-03804 from the Swedish Research Council. M.B. acknowledges support from the Slovenian national research agency ARRS through grant N1-0238. T.A.H. is supported by an appointment to the NASA Postdoctoral Program (NPP) at NASA Goddard Space Flight Center, administered by Oak Ridge Associated Universities under contract with NASA. A.Z. and L.J.F. acknowledge support by grant No. 2020750 from the United States-Israel Binational Science Foundation (BSF) and grant No. 2109066 from the United States National Science Foundation (NSF), and by the Ministry of Science & Technology, Israel. E. V. acknowledges financial support through grants PRIN-MIUR 2017WSCC32 and 2020SKSTHZ and INAF “main-stream” grants 1.05.01.86.20 and 1.05.01.86.31. E.V. acknowledges support from the INAF GO grant 2022 “The revolution is around the corner: JWST will probe globular cluster precursors and Population III stellar clusters at cosmic dawn.” A.C.C. thanks the Leverhulme Trust for their support via a Leverhulme Early Career Fellowship.

Facilities: JWST (NIRCam, NIRSpec), and HST (ACS, WFC3).

Software: STScI JWST pipeline, MSAEXP, GRIZLI (Brammer et al. 2022), EAZY (Brammer et al. 2008), ASTROPY (Astropy Collaboration et al. 2013, 2018, 2022), PHOTUTILS (Bradley et al. 2023), PIXEDFIT (Abdurro’uf et al. 2021, 2022), BAGPIPES (Carnall et al. 2018, 2019), BEAGLE (Chevallard & Charlot 2016), CLOUDY (Ferland et al. 1998, 2013, 2017), PYNEB (Luridiana et al. 2015), and HII-CHI-MISTRY (Pérez-Montero 2014).

ORCID iDs

Tiger Yu-Yang Hsiao  <https://orcid.org/0000-0003-4512-8705>
 Abdurro’uf  <https://orcid.org/0000-0002-5258-8761>
 Dan Coe  <https://orcid.org/0000-0001-7410-7669>
 Rebecca L. Larson  <https://orcid.org/0000-0003-2366-8858>
 Intae Jung  <https://orcid.org/0000-0003-1187-4240>
 Matilde Mingozi  <https://orcid.org/0000-0003-2589-762X>
 Pratika Dayal  <https://orcid.org/0000-0001-8460-1564>

Nimisha Kumari  <https://orcid.org/0000-0002-5320-2568>
 Vasily Kokorev  <https://orcid.org/0000-0002-5588-9156>
 Anton Vikaeus  <https://orcid.org/0000-0002-4853-1076>
 Gabriel Brammer  <https://orcid.org/0000-0003-2680-005X>
 Lukas J. Furtak  <https://orcid.org/0000-0001-6278-032X>
 Angela Adamo  <https://orcid.org/0000-0002-8192-8091>
 Felipe Andrade-Santos  <https://orcid.org/0000-0002-8144-9285>
 Jacqueline Antwi-Danso  <https://orcid.org/0000-0002-0243-6575>
 Maruša Bradač  <https://orcid.org/0000-0001-5984-0395>
 Larry D. Bradley  <https://orcid.org/0000-0002-7908-9284>
 Tom Broadhurst  <https://orcid.org/0000-0002-8785-8979>
 Adam C. Carnall  <https://orcid.org/0000-0002-1482-5818>
 Christopher J. Conselice  <https://orcid.org/0000-0003-1949-7638>
 Jose M. Diego  <https://orcid.org/0000-0001-9065-3926>
 Megan Donahue  <https://orcid.org/0000-0002-2808-0853>
 Jan J. Eldridge  <https://orcid.org/0000-0002-1722-6343>
 Seiji Fujimoto  <https://orcid.org/0000-0001-7201-5066>
 Alaina Henry  <https://orcid.org/0000-0002-6586-4446>
 Svea Hernandez  <https://orcid.org/0000-0003-4857-8699>
 Taylor A. Hutchison  <https://orcid.org/0000-0001-6251-4988>
 Bethan L. James  <https://orcid.org/0000-0003-4372-2006>
 Colin Norman  <https://orcid.org/0000-0002-5222-5717>
 Hyunbae Park  <https://orcid.org/0000-0002-7464-7857>
 Norbert Pirzkal  <https://orcid.org/0000-0003-3382-5941>
 Marc Postman  <https://orcid.org/0000-0002-9365-7989>
 Massimo Ricotti  <https://orcid.org/0000-0003-4223-7324>
 Jane R. Rigby  <https://orcid.org/0000-0002-7627-6551>
 Eros Vanzella  <https://orcid.org/0000-0002-5057-135X>
 Brian Welch  <https://orcid.org/0000-0003-1815-0114>
 Stephen M. Wilkins  <https://orcid.org/0000-0003-3903-6935>
 Rogier A. Windhorst  <https://orcid.org/0000-0001-8156-6281>
 Xinfeng Xu  <https://orcid.org/0000-0002-9217-7051>
 Erik Zackrisson  <https://orcid.org/0000-0003-1096-2636>
 Adi Zitrin  <https://orcid.org/0000-0002-0350-4488>

References

- Abdurro’uf, Coe, D., Jung, I., et al. 2023, *ApJ*, 945, 117
 Abdurro’uf, Lin, Y.-T., Wu, P.-F., & Akiyama, M. 2021, *ApJS*, 254, 15
 Abdurro’uf, Lin, Y.-T., Wu, P.-F., & Akiyama, M. 2022, piXedfit: Analyze spatially resolved SEDs of galaxies, Astrophysics Source Code Library, ascl:2207.033
 Arrabal Haro, P., Dickinson, M., Finkelstein, S. L., et al. 2023a, *Natur*, 622, 707
 Arrabal Haro, P., Dickinson, M., Finkelstein, S. L., et al. 2023b, *ApJL*, 951, L22
 Asplund, M., Amarsi, A. M., & Grevesse, N. 2021, *A&A*, 653, A141
 Astropy Collaboration, Price-Whelan, A. M., Lim, P. L., et al. 2022, *ApJ*, 935, 167
 Astropy Collaboration, Price-Whelan, A. M., Sipőcz, B. M., et al. 2018, *AJ*, 156, 123
 Astropy Collaboration, Robitaille, T. P., Tollerud, E. J., et al. 2013, *A&A*, 558, A33
 Bañados, E., Venemans, B. P., Mazzucchelli, C., et al. 2018, *Natur*, 553, 473
 Barkana, R., & Loeb, A. 2001, *PhR*, 349, 125
 Baskin, A., & Laor, A. 2005, *MNRAS*, 356, 1029
 Berg, D. A., Erb, D. K., Henry, R. B. C., Skillman, E. D., & McQuinn, K. B. W. 2019, *ApJ*, 874, 93
 Berg, D. A., James, B. L., King, T., et al. 2022, *ApJS*, 261, 31
 Binggeli, C., Zackrisson, E., Ma, X., et al. 2019, *MNRAS*, 489, 3827
 Böker, T., Beck, T. L., Birkmann, S. M., et al. 2023, *PASP*, 135, 038001
 Bouwens, R. J., Smit, R., Labbé, I., et al. 2016, *ApJ*, 831, 176
 Boyer, M. L., Anderson, J., Gennaro, M., et al. 2022, *RNAAS*, 6, 191
 Boyett, K., Trenti, M., Leethochawalit, N., et al. 2024, *NatAs*, 8, 657
 Bradley, L. D., Coe, D., Brammer, G., et al. 2023, *ApJ*, 955, 13

- Brammer, G., Strait, V., Matharu, J., & Momcheva, I. 2022, *grizli*, v1.5.0, Zenodo, doi:10.5281/zenodo.6672538
- Brammer, G. B., van Dokkum, P. G., & Coppi, P. 2008, *ApJ*, **686**, 1503
- Brunton, S., Lin, Y.-H., Scarlata, C., & Hayes, M. J. 2023, *ApJL*, **949**, L40
- Bunker, A. J., Saxena, A., Cameron, A. J., et al. 2023, *A&A*, **677**, A88
- Cameron, A. J., Katz, H., Rey, M. P., & Saxena, A. 2023a, *MNRAS*, **523**, 3516
- Cameron, A. J., Saxena, A., Bunker, A. J., et al. 2023b, *A&A*, **677**, A115
- Carnall, A. C., McLure, R. J., Dunlop, J. S., & Davé, R. 2018, *MNRAS*, **480**, 4379
- Carnall, A. C., McLure, R. J., Dunlop, J. S., et al. 2019, *MNRAS*, **490**, 417
- Chabrier, G. 2003, *PASP*, **115**, 763
- Chan, B. M. Y., Broadhurst, T., Lim, J., et al. 2017, *ApJ*, **835**, 44
- Charbonnel, C., Schaerer, D., Prantzos, N., et al. 2023, *A&A*, **673**, L7
- Charlot, S., & Fall, S. M. 2000, *ApJ*, **539**, 718
- Chevallard, J., & Charlot, S. 2016, *MNRAS*, **462**, 1415
- Chisholm, J., Rigby, J. R., Bayliss, M., et al. 2019, *ApJ*, **882**, 182
- Christensson, L., Richard, J., Hjorth, J., et al. 2012, *MNRAS*, **427**, 1953
- Coe, D., Umetsu, K., Zitrin, A., et al. 2012, *ApJ*, **757**, 22
- Coe, D., Zitrin, A., Carrasco, M., et al. 2013, *ApJ*, **762**, 32
- Conroy, C., Gunn, J. E., & White, M. 2009, *ApJ*, **699**, 486
- Curtis-Lake, E., Carniani, S., Cameron, A., et al. 2023, *NatAs*, **7**, 622
- Davies, F. B., Hennawi, J. F., Bañados, E., et al. 2018, *ApJ*, **864**, 142
- Díaz, A. I., Castellanos, M., Terlevich, E., & Luisa García-Vargas, M. 2000, *MNRAS*, **318**, 462
- Dijkstra, M. 2014, *PASA*, **31**, e040
- Dopita, M. A., & Sutherland, R. S. 2003, *Astrophysics of the Diffuse Universe* (Berlin: Springer)
- Ebeling, H., Barrett, E., Donovan, D., et al. 2007, *ApJL*, **661**, L33
- Erb, D. K., Shapley, A. E., Steidel, C. C., et al. 2003, *ApJ*, **591**, 101
- Ferland, G. J., Chatzikos, M., Guzmán, F., et al. 2017, *RMxAA*, **53**, 385
- Ferland, G. J., Korista, K. T., Verner, D. A., et al. 1998, *PASP*, **110**, 761
- Ferland, G. J., Porter, R. L., van Hoof, P. A. M., et al. 2013, *RMxAA*, **49**, 137
- Ferruit, P., Jakobsen, P., Giardino, G., et al. 2022, *A&A*, **661**, A81
- Flury, S. R., Jaskot, A. E., Ferguson, H. C., et al. 2022, *ApJS*, **260**, 1
- Fujimoto, S., Arrabal Haro, P., Dickinson, M., et al. 2023, *ApJL*, **949**, L25
- Furtak, L. J., Shuntov, M., Atek, H., et al. 2023, *MNRAS*, **519**, 3064
- Gaia Collaboration, Brown, A. G. A., Vallenari, A., et al. 2021, *A&A*, **649**, A1
- Gardner, J. P., Mather, J. C., Abbott, R., et al. 2023, *PASP*, **135**, 1048
- Garnett, D. R. 1989, *ApJ*, **345**, 282
- Glazebrook, K., Blake, C., Economou, F., Lilly, S., & Colless, M. 1999, *MNRAS*, **306**, 843
- Groves, B., Brinchmann, J., & Walcher, C. J. 2012, *MNRAS*, **419**, 1402
- Gutkin, J., Charlot, S., & Bruzual, G. 2016, *MNRAS*, **462**, 1757
- Harikane, Y., Nakajima, K., Ouchi, M., et al. 2024, *ApJ*, **960**, 56
- Heintz, K. E., Watson, D., Brammer, G., et al. 2024, *Sci*, **384**, 890
- Hicks, E. K. S., Malkan, M. A., Teplitz, H. I., McCarthy, P. J., & Yan, L. 2002, *ApJ*, **581**, 205
- Hoffmann, S. L., Mack, J., Avila, R., et al. 2021, *AAS Meeting Abstracts*, **53**, 216.02
- Home, K. 1986, *PASP*, **98**, 609
- Hsiao, T. Y.-Y., Coe, D., Abdurro'uf, et al. 2023, *ApJL*, **949**, L34
- Hutchison, T. A., Papovich, C., Finkelstein, S. L., et al. 2019, *ApJ*, **879**, 70
- Hutter, A., Dayal, P., Partl, A. M., & Müller, V. 2014, *MNRAS*, **441**, 2861
- Inoue, A. K., Shimizu, I., Iwata, I., & Tanaka, M. 2014, *MNRAS*, **442**, 1805
- Izotov, Y. I., Thuan, T. X., & Guseva, N. G. 2021, *MNRAS*, **504**, 3996
- Izotov, Y. I., Worseck, G., Schaerer, D., et al. 2018, *MNRAS*, **478**, 4851
- Jakobsen, P., Ferruit, P., Alves de Oliveira, C., et al. 2022, *A&A*, **661**, A80
- Jaskot, A. E., & Oey, M. S. 2013, *ApJ*, **766**, 91
- Jaskot, A. E., & Ravindranath, S. 2016, *ApJ*, **833**, 136
- Jung, I., Finkelstein, S. L., Arrabal Haro, P., et al. 2024, *ApJ*, **967**, 73
- Jung, I., Finkelstein, S. L., Song, M., et al. 2017, *ApJ*, **834**, 81
- Kennicutt, R. C., Jr 1998, *ARA&A*, **36**, 189
- Kewley, L. J., Nicholls, D. C., & Sutherland, R. S. 2019, *ARA&A*, **57**, 511
- Koekemoer, A. M., Fruchter, A. S., Hook, R. N., & Hack, W. 2003, in *HST Calibration Workshop : Hubble after the Installation of the ACS and the NICMOS Cooling System* (Baltimore, MD: STScI), 337
- Kroupa, P. 2001, *MNRAS*, **322**, 231
- Kroupa, P., Tout, C. A., & Gilmore, G. 1993, *MNRAS*, **262**, 545
- Lam, D., Bouwens, R. J., Coe, D., et al. 2019, arXiv:1903.08177
- Le Fèvre, O., Lemaux, B. C., Nakajima, K., et al. 2019, *A&A*, **625**, A51
- Leitherer, C., Schaerer, D., Goldader, J. D., et al. 1999, *ApJS*, **123**, 3
- Leja, J., Johnson, B. D., Conroy, C., van Dokkum, P. G., & Byler, N. 2017, *ApJ*, **837**, 170
- Levesque, E. M., & Richardson, M. L. A. 2014, *ApJ*, **780**, 100
- Luridiana, V., Morisset, C., & Shaw, R. A. 2015, *A&A*, **573**, A42
- Madau, P., & Dickinson, M. 2014, *ARA&A*, **52**, 415
- Mainali, R., Kollmeier, J. A., Stark, D. P., et al. 2017, *ApJL*, **836**, L14
- Mainali, R., Stark, D. P., Tang, M., et al. 2020, *MNRAS*, **494**, 719
- Maiolino, R., & Mannucci, F. 2019, *A&ARv*, **27**, 3
- Mason, C. A., & Gronke, M. 2020, *MNRAS*, **499**, 1395
- Mason, C. A., Treu, T., Dijkstra, M., et al. 2018, *ApJ*, **856**, 2
- Meena, A. K., Zitrin, A., Jiménez-Teja, Y., et al. 2023, *ApJL*, **944**, L6
- Mingozzi, M., James, B. L., Arellano-Córdova, K. Z., et al. 2022, *ApJ*, **939**, 110
- Miralda-Escudé, J. 1998, *ApJ*, **501**, 15
- Mortlock, D. J., Warren, S. J., Venemans, B. P., et al. 2011, *Natur*, **474**, 616
- Nakajima, K., Ouchi, M., Isobe, Y., et al. 2023, *ApJS*, **269**, 33
- Nakajima, K., Ouchi, M., Xu, Y., et al. 2022, *ApJS*, **262**, 3
- Oesch, P. A., Brammer, G., van Dokkum, P. G., et al. 2016, *ApJ*, **819**, 129
- Osterbrock, D. E. 1989, *Astrophysics of Gaseous Nebulae and Active Galactic Nuclei* (Mill Valley, CA: Univ. Science Books)
- Park, H., Jung, I., Song, H., et al. 2021, *ApJ*, **922**, 263
- Peimbert, M. 1967, *ApJ*, **150**, 825
- Pérez-Montero, E. 2014, *MNRAS*, **441**, 2663
- Pérez-Montero, E., Hägele, G. F., Contini, T., & Díaz, Á. 2007, *MNRAS*, **381**, 125
- Pirzkal, N., Coe, D., Frye, B. L., et al. 2015, *ApJ*, **804**, 11
- Reddy, N. A., Shapley, A. E., Sanders, R. L., et al. 2018, *ApJ*, **869**, 92
- Reddy, N. A., Steidel, C. C., Pettini, M., et al. 2008, *ApJS*, **175**, 48
- Rieke, M. J., Kelly, D. M., Misselt, K., et al. 2023, *PASP*, **135**, 028001
- Rigby, J., Perrin, M., McElwain, M., et al. 2023, *PASP*, **135**, 048001
- Rigby, J. R., Bayliss, M. B., Gladders, M. D., et al. 2015, *ApJL*, **814**, L6
- Roberts-Borsani, G., Treu, T., Chen, W., et al. 2023, *Natur*, **618**, 480
- Robertson, B. E., Furlanetto, S. R., Schneider, E., et al. 2013, *ApJ*, **768**, 71
- Sadoun, R., Zheng, Z., & Miralda-Escudé, J. 2017, *ApJ*, **839**, 44
- Salim, S., Boquien, M., & Lee, J. C. 2018, *ApJ*, **859**, 11
- Sanders, R. L., Shapley, A. E., Topping, M. W., Reddy, N. A., & Brammer, G. B. 2024, *ApJ*, **962**, 24
- Schaerer, D. 2003, *A&A*, **397**, 527
- Shapiro, P. R., & Giroux, M. L. 1987, *ApJL*, **321**, L107
- Shapley, A. E., Sanders, R. L., Reddy, N. A., Topping, M. W., & Brammer, G. B. 2023, *ApJ*, **954**, 157
- Smith, A., Kannan, R., Garaldi, E., et al. 2022, *MNRAS*, **512**, 3243
- Stanway, E. R., & Eldridge, J. J. 2018, *MNRAS*, **479**, 75
- Stark, D. P., Ellis, R. S., Charlot, S., et al. 2017, *MNRAS*, **464**, 469
- Steidel, C. C., Strom, A. L., Pettini, M., et al. 2016, *ApJ*, **826**, 159
- Storey, P. J., & Zeppen, C. J. 2000, *MNRAS*, **312**, 813
- Tacchella, S., Eisenstein, D. J., Hainline, K., et al. 2023, *ApJ*, **952**, 74
- Tang, M., Stark, D. P., Chen, Z., et al. 2023, *MNRAS*, **526**, 1657
- Tang, M., Stark, D. P., Chevallard, J., & Charlot, S. 2019, *MNRAS*, **489**, 2572
- Tang, M., Stark, D. P., Chevallard, J., et al. 2021, *MNRAS*, **501**, 3238
- Tasitsiomi, A. 2006, *ApJ*, **645**, 792
- Treu, T., Schmidt, K. B., Trenti, M., Bradley, L. D., & Stiavelli, M. 2013, *ApJL*, **775**, L29
- Ucci, G., Dayal, P., Hutter, A., et al. 2023, *MNRAS*, **518**, 3557
- Vanzella, E., Caminha, G. B., Calura, F., et al. 2020, *MNRAS*, **491**, 1093
- Vanzella, E., Claeysens, A., Welch, B., et al. 2023, *ApJ*, **945**, 53
- Wang, F., Davies, F. B., Yang, J., et al. 2020, *ApJ*, **896**, 23
- Weinberger, L. H., Kulkarni, G., Haehnelt, M. G., Choudhury, T. R., & Puchwein, E. 2018, *MNRAS*, **479**, 2564
- Wilkins, S. M., Feng, Y., Di-Matteo, T., et al. 2016, *MNRAS*, **458**, L6
- Wilkins, S. M., Lovell, C. C., & Stanway, E. R. 2019, *MNRAS*, **490**, 5359
- Williams, H., Kelly, P. L., Chen, W., et al. 2023, *Sci*, **380**, 416
- Witstok, J., Smit, R., Maiolino, R., et al. 2021, *MNRAS*, **508**, 1686
- Yang, J., Wang, F., Fan, X., et al. 2020, *ApJL*, **897**, L14